Stratospheric aerosol data records for the climate change initiative : Development, validation and application to chemistry-climate modelling

Bingen, Christine

2017-12-15

Bingen , C , Robert , C E , Stebel , K , Bruehl , C , Schallock , J , Vanhellemont , F , Mateshvili , N , Hoepfner , M , Trickl , T , Barnes , J E , Jumelet , J , Vernier , J-P , Popp , T , de Leeuw , G & Pinnock , S 2017 , ' Stratospheric aerosol data records for the climate change initiative : Development, validation and application to chemistry-climate modelling ' , Remote Sensing of Environment , vol. 203 , pp. 296-321 . https://doi.org/10.1016/j.rse.2017.06.002

http://hdl.handle.net/10138/231503
https://doi.org/10.1016/j.rse.2017.06.002

Remote Sensing of Environment 203 (2017) 296–321

Contents lists available at ScienceDirect

Remote Sensing of Environment

journal homepage: www.elsevier.com/locate/rse

Stratospheric aerosol data records for the climate change initiative: Development, validation and application to chemistry-climate modelling

Christine Bingen [a,*], Charles E. Robert [a], Kerstin Stebel [b], Christoph Brühl [c], Jennifer Schallock [c], Filip Vanhellemont [a], Nina Mateshvili [a], Michael Höpfner [d], Thomas Trickl [e], John E. Barnes [f], Julien Jumelet [g], Jean-Paul Vernier [h,i], Thomas Popp [j], Gerrit de Leeuw [k,l], Simon Pinnock [m]

[a] Royal Belgian Institute for Space Aeronomy, B-1180 Brussels, Belgium
[b] Norwegian Institute for Air Research, N-2027 Kjeller, Norway
[c] Max Planck-Institute for Chemistry, D-55020 Mainz, Germany
[d] Institute of Meteorology and Climate Research, Karlsruhe Institute of Technology, IMK-ASF, Karlsruhe, Germany
[e] Institute of Meteorology and Climate Research, Karlsruhe Institute of Technology, IMK-IFU, Garmisch-Partenkirchen, Germany
[f] National Oceanic and Atmospheric Administration, Earth System Research Laboratory, Global Monitoring Division, Mauna Loa Observatory, USA
[g] LATMOS, Institut Pierre Simon Laplace, Université Versailles Saint-Quentin-en-Yvelines, Université Pierre et Marie Curie - Sorbonne Universités, Paris 06, CNRS, Guyancourt, France
[h] Science Systems and Applications, Inc., Hampton, VA, USA
[i] NASA Langley Research Center, Hampton, VA, USA
[j] Deutsches Zentrum für Luft- und Raumfahrt e. V., Deutsches Fernerkundungsdatenzentrum (DFD), 82234 Oberpfaffenhofen, Germany
[k] Finnish Meteorological Institute (FMI), Climate Research Unit, 00101 Helsinki, Finland
[l] Department of Physics, University of Helsinki, 00014 Helsinki, Finland
[m] ESA ECSAT, Didcot OX11 0FD, UK

ARTICLE INFO

Article history:
Received 25 October 2016
Received in revised form 15 May 2017
Accepted 2 June 2017
Available online 8 July 2017

Keywords:
Stratospheric aerosol extinction
Aerosol remote sensing
Climate data record
Volcanic eruptions
Aerosol burden
Climate modelling
Lidar
GOMOS
ENVISAT

ABSTRACT

This paper presents stratospheric aerosol climate records developed in the framework of the Aerosol_cci project, one of the 14 parallel projects from the ESA Climate Change Initiative. These data records were processed from a stratospheric aerosol dataset derived from the GOMOS experiment, using an inversion algorithm optimized for aerosol retrieval, called AerGOM. They provide a suite of aerosol parameters, such as the aerosol extinction coefficient at different wavelengths in the UV–visible range. The extinction record includes the total extinction as well as separate fields for liquid sulfate aerosols and polar stratospheric clouds (PSCs). Several additional fields (PSC flag, etc.) are also provided. The resulting stratospheric aerosol dataset, which spans the whole duration of the GOMOS mission (2002 − 2012), was validated using different reference datasets (lidar and balloon profiles).

In the present paper, the emphasis is put on the extinction records. After a thorough analysis of the original AerGOM dataset, we describe the methodology used to construct the gridded CCI-GOMOS dataset and the resulting improvements on both the AerGOM algorithm and the binning procedure, in terms of spatio-temporal resolution, coverage and data quality.

The extinction datasets were validated using lidar profiles from three ground-based stations (Mauna Loa, Garmisch-Partenkirchen, Dumont d'Urville). The median difference of the CCI-GOMOS (Level 3) extinction and ground-based lidar profiles is between ~15% and ~45% in the 16–21 km altitude range, depending on the considered site and aerosol type.

The CCI-GOMOS dataset was subsequently used, together with a MIPAS SO_2 time series, to update a volcanic eruption inventory published previously, thus providing a more comprehensive list of eruptions for the ENVISAT period (2002–2012). The number of quantified eruptions increases from 102 to 230 in the updated inventory. This new inventory was used to simulate the evolution of the global radiative forcing by application of the EMAC chemistry-climate model. Results of this simulation improve the agreement between modelled global radiative forcing of stratospheric aerosols at about 100 hPa compared to values estimated from observations. Medium eruptions like the ones of Soufriere Hills/Rabaul (2006), Sarychev (2009) and Nabro (2011) cause a forcing change from about -0.1 W/m^2 to -0.2 W/m^2.

* Corresponding author.
E-mail address: Christine.Bingen@aeronomie.be (C. Bingen).

http://dx.doi.org/10.1016/j.rse.2017.06.002

1. Introduction

Stratospheric aerosols are a major actor of climate: they play an important role in stratospheric ozone physico-chemistry and affect the propagation of light in the atmosphere. They also contribute to the formation of polar stratospheric clouds (PSCs) responsible for ozone depletion in the polar regions during springtime. Although carbonyl sulfide (OCS) produced by the oceans is also an important natural source of this kind of particles (Brühl et al., 2012) and the contribution of organic materials in radiative forcing has been recently emphasized (Yu et al., 2016), stratospheric aerosols mainly originate from volcanic sources, either by direct injection of SO_2 during major eruptions or by transport from the troposphere through the tropopause. This transport occurs mainly in the tropics following the general Brewer-Dobson circulation, but other specific pathways have recently been identified, in particular the summer Asian monsoon (Vernier et al., 2011a, 2011b, 2015). A detailed overview of the current knowledge about stratospheric aerosols and remaining issues can be found in (SPARC, 2006) and (Kremser et al., 2016).

The role of volcanoes in feeding the stratospheric aerosol layer (the so-called Junge layer) is substantial. The volcanic load in the stratosphere has varied over time scales from weeks to decades, and since the beginning of Earth observation from space, the aerosol concentration varied over several orders of magnitude. The Pinatubo eruption in June 1991 was an important event during which about 17.000 kt SO_2 was injected into the stratosphere (e.g. Brühl et al., 2015), which represents about 60 times the estimated level of nonvolcanic aerosol (Kremser et al., 2016). After a long relaxation time of >5 years, the stratosphere reached a state of historically low aerosol load of around 1999–2000. After this period, a gradual increase of the aerosol burden was observed in the tropics. Several effects have been identified as causes of this new increase: a succession of tropical eruptions of medium intensity (Vernier et al., 2011b), but also anthropogenic sources such as the Asian sulfur emissions (Hofmann et al., 2009). Vernier et al. (2011a) observed an Asian tropical aerosol layer linked with the monsoon system, which transports Asian pollution to the upper troposphere and lower stratosphere.

Despite the numerous studies dedicated to the evolution of the atmosphere in the post-2000 period, many aspects remain uncertain, such as the respective roles of volcanic and anthropogenic sources in the evolution of the aerosol load. Discrepancies remain between climate model projections and estimates of the radiative forcing from satellite measurements (Solomon et al., 2011). The reasons for these discrepancies have to be clarified. It is of utmost importance to understand the processes and transport patterns, to identify aerosol sources and quantify their strength in a reliable way. Besides high performance climate models, reliable datasets are needed to constrain these models and to validate their projections.

The development of such datasets on a global scale relies on long-term satellite missions able to provide measurements with good temporal and spatial resolution and coverage. For the considered period, several instruments can be used such as the Optical Spectrograph and InfraRed Imaging Sensor (OSIRIS) launched in 2001 onboard ODIN (Bourassa et al., 2007), the Scanning Imaging Absorption spectroMeter for Atmospheric ChartographY (SCIAMACHY) launched onboard ENVISAT (von Savigny et al., 2015). In this work, we make use of the Global Ozone Monitoring by Occultation of Stars (GOMOS) experiment, also launched onboard ENVISAT and providing global measurements over the period 2002–2012.

It is the ultimate objective of the Aerosol_cci project (Popp et al., 2016), part of the Climate Change Initiative (CCI) of the European Space Agency (ESA) (Hollmann et al., 2013), to quantify the global aerosol distribution in the atmosphere (particularly in the troposphere and stratosphere) and their variability.

The aim of ESA's CCI is to develop Climate Data Records (CDR) from ESA space remote sensing experiments for the main Essential Climate Variables (ECV) identified by the Intergovernmental Panel on Climate Change (IPCC). Based on global observations of the Earth's atmosphere, such CDRs are needed, among other applications, to constrain and validate climate models. This task requires data with a good coverage, high quality, and a precision and accuracy according to the current standard and needs of state-of-the-art climate models. To achieve these performances, each CCI project relies upon a specific User community, endorsing the role of an independent validation team and providing recommendations and requirements. The requirements formulated by the Global Climate Observation System (GCOS, 2009, 2011) provide a reference framework in terms of parameters needed by the Climate Community, grid resolution, and data accuracy and stability. GCOS requirements for stratospheric aerosol extinction coefficient are given in Table 1.

A detailed overview of the general approach recommended to produce consistent aerosol climate data records and lessons learned within the Aerosol_cci project can be found in (Popp et al., 2016), where both tropospheric and stratospheric aspects are addressed. In the present work, the focus is exclusively on the stratospheric aerosol extinction coefficient CDR (we will use the shortcut "aerosol extinction CDR" in the following) derived from the AerGOM algorithm. The retrieval of particle size information and related CDRs, which are still under development, will be the subject of a future publication.

The SPARC (Stratosphere-troposphere Processes And their Role in Climate) Community represents the Climate Modelling Community for the stratospheric aspects of Aerosol_cci. The User and Validation teams not only uses the produced data records and benchmarks them against other available datasets and model projections, but also performs the validation tasks, using in-situ and ground-based datasets. Although such measurements provide data over a limited geographical extent, they are based on different techniques resulting in validation data which are different regarding their limitations and biases. For this reason, lidar time series and balloon-borne campaigns (optical particle counting) are useful data sources for the validation of stratospheric data records.

In this paper, we present new gridded stratospheric aerosol extinction datasets developed for chemistry-climate modelling applications using the GOMOS experiment. Therefore, we use the vertical extinction profiles retrieved using AerGOM, a recent alternative retrieval algorithm optimized for aerosol retrieval. We describe the development of this CDR, its validation, and its contribution to the assessment of the volcanic contribution to the aerosol burden during the post-2000 time period. More specifically, we present the update of an inventory of volcanic eruptions published previously (Brühl et al., 2015), and its use to determine more accurately the radiative forcing by stratospheric aerosols during the period 2002–2012, by numerical simulations using the EMAC chemistry climate model. Here, GOMOS is also used for validation and further development of the aerosol model.

The paper is organized as follows: After presenting shortly the GOMOS experiments and the AerGOM retrieval algorithm in Chapter 2, we describe in Chapter 3 the processing of the CCI-GOMOS time series (Level 3) from the AerGOM dataset (Level 2). We show how we

Table 1
Target requirements provided by GCOS for the aerosol extinction coefficient from the troposphere to at least 35 km (GCOS, 2011).

Parameter	Horizontal resolution	Vertical resolution	Temporal resolution	Accuracy	Stability
Aerosol extinction coefficient	200–500 km	<1 km near tropopause ~2 km in the middle stratosphere	Weekly	10%	20%

improved the extinction retrieval by AerGOM and how an appropriate selection of the star and occultation parameters increased the quality of the CCI-GOMOS time series. Chapter 4 presents the gradual improvement of the CCI-GOMOS data records, highlighting the evolution of the CDR features along the main versions to better meet the needs of the modelling community. Validation aspects are detailed in Chapter 5. Finally, Chapter 6 presents the use of the CCI-GOMOS data records in the update of the inventory of volcanic eruptions.

2. Aerosol retrieval from GOMOS

2.1. The GOMOS instrument

The GOMOS instrument was launched on March 1st, 2002 onboard ENVISAT in a sunsynchronous orbit, and provided about 10 years of data until the contact with ENVISAT was lost on April 8th, 2012. GOMOS is based on the stellar occultation principle. The abundance of stars (about 300 stars selected for use by GOMOS) results in a dramatic increase of the measurement rate with respect to solar occultation measurements. However, scintillation effects affect the weak light beam from the star during its propagation through the Earth's atmosphere, resulting in a limited signal-to noise ratio, which depends on the star properties (magnitude and temperature) and on the orbital parameters, such as its obliquity and the solar zenith angle. GOMOS is equipped with two spectrometers: spectrometer SPA, which measures in the UV–visible, covering the range 248–690 nm with a sampling resolution of 0.312 nm, and spectrometer SPB which measures in the near infrared and is split in two parts, SPB1 and SPB2 covering the ranges 755–774 nm and 926–954 nm respectively. The spectral resolution is 0.8 nm for SPA and 0.13 nm for SPB. Two broadband fast photometers measuring in the red (646–698 nm) and in the blue (473–527 nm) are used to remove scintillation effects during data processing (Sofieva et al., 2009). The GOMOS instrument, measurement principle and data retrieval have been described in a comprehensive way by Bertaux et al. (2010) (see also references therein).

2.2. The AerGOM algorithm.

The nominal retrieval algorithm developed for GOMOS, IPF (Instrument Processor Facility), demonstrated its ability to retrieve successfully vertical density profiles of O_3, NO_2, NO_3 (Kyrölä et al., 2008, 2010), as well as aerosol extinction profiles at 500 nm (Vanhellemont et al., 2008). However, the performances of the parameterization used for the aerosol spectral dependence appeared to be particularly poor, and the extinction coefficient calculated at other wavelengths than the 500 nm reference is often very noisy (Vanhellemont et al., 2016).

Learning from the problems encountered in IPF, a new retrieval algorithm called AerGOM was developed, having as primary objective the improvement of the aerosol retrieval and its spectral dependence. One of the main improvements brought to AerGOM is a revision of the aerosol spectral parameterization to resolve scaling problems and better constrain the spectral inversion. The new formulation of the spectral model for the slant optical thickness τ as a function of the wavelength λ is a polynomial with degree m of some function $f(\lambda)$ written in the form:

$$\tau(\lambda) = \sum_{i=1}^{m+1} q_i(\lambda) \times \tau(\lambda_i) \tag{1}$$

with

$$q_i = \prod_{j\neq i; j=1}^{m+1} \frac{f(\lambda) - f(\lambda_j)}{f(\lambda_i) - f(\lambda_j)} \tag{2}$$

based on $m + 1$ reference wavelengths λ_i. Several choices of $f(\lambda)$ are possible, such as a simple linear function $f(\lambda) = \lambda$, or the inverse function $f(\lambda) = \lambda^{-1}$. In the current version of AerGOM, we use, for Eq. (1), a second degree polynomial ($m = 2$) in the inverse wavelength, $f(\lambda) = \lambda^{-1}$:

$$\begin{aligned}\tau(\lambda) = &\frac{\lambda^{-1}-\lambda_2{}^{-1}}{\lambda_1{}^{-1}-\lambda_2{}^{-1}} \cdot \frac{\lambda^{-1}-\lambda_3{}^{-1}}{\lambda_1{}^{-1}-\lambda_3{}^{-1}} \cdot \tau(\lambda_1)\\ &+\frac{\lambda^{-1}-\lambda_1{}^{-1}}{\lambda_2{}^{-1}-\lambda_1{}^{-1}} \cdot \frac{\lambda^{-1}-\lambda_3{}^{-1}}{\lambda_2{}^{-1}-\lambda_3{}^{-1}} \cdot \tau(\lambda_2)\\ &+\frac{\lambda^{-1}-\lambda_1{}^{-1}}{\lambda_3{}^{-1}-\lambda_1{}^{-1}} \cdot \frac{\lambda^{-1}-\lambda_2{}^{-1}}{\lambda_3{}^{-1}-\lambda_2{}^{-1}} \cdot \tau(\lambda_3)\end{aligned} \tag{3}$$

The reference wavelengths λ_1, λ_2, and λ_3 are chosen equal to 350, 550, and 756 nm, respectively. From preliminary comparisons with the Stratospheric Aerosol and Gas Experiment (SAGE) II and III extinction datasets, Robert et al. (2016) found that a linear dependence ($m = 1$) might be a better choice than the quadratic one used here. However, the improvements brought to AerGOM (See more particularly Section 2.3) improve the agreement between AerGOM and those datasets, and since the more versatile choice of a quadratic law might be more adequate for the use of extinction spectra in the retrieval of particle size distributions, we chose, at this stage, to keep this choice of parameterization.

A detailed description of the AerGOM algorithm, version 1.0 and of the main differences and improvements with respect to IPF is given in (Vanhellemont et al., 2016). In the present work, we make use of version 2.0 where the most important change with respect to version 1.0 concerns some improvement of the optimization process, and the update of the cross-sections. Both aspects are described below. Further, version 2.0 was extended to version 3.0 to provide additional aerosol parameters, most of them related to size distribution retrieval. These two last versions (2.0 and 3.0) are very similar concerning extinction retrieval and can be considered as equivalent in this respect. The use of the various versions in the present work is specified in Section 4.

2.3. Quality of the optimization process

Initially, the quality of the aerosol records appeared to be affected by the occurrence of a number of anomalous profiles characterized by an abnormally high value of the extinction coefficient in the range 20–40 km altitude, and by an inversion of the slope of the spectral dependence. This odd behaviour, discussed in Robert et al. (2016), occurred typically for dim cool star occultations and was due to the poor information content of this kind of occultations, especially at high altitudes where the aerosol load is very low, and its effect on the radiation very weak. The problem was solved by using, as first guess for the non-linear optimization of the spectral retrieval, climatological data for the gas and aerosol species which prevent the iterative process to converge far from a realistic solution. The resolution of this problem allowed a significant relaxation of the selection criteria imposed on the star properties.

2.4. Choice of the gas absorption cross-sections

Another problem encountered was the frequent occurrence of negative values of the aerosol extinction coefficient, especially above about 30 km altitude. This issue was particularly pronounced at the longest wavelengths (about 700–750 nm). Although stray light contamination was suspected at first to be the main reason for these unphysical values, it appeared, after analysis of the cross-section database, that some gas cross-section spectra used for the retrieval of the gas species by AerGOM were not optimal in terms of available spectral range and temperature dependence. Hence, the problem could finally be controlled by a revision of the molecular absorption cross-section spectra used for the retrieval. To this end, the most recent absorption cross-section measurements for the gases of interest were investigated to improve the spectral range, the temperature dependence and the consistency

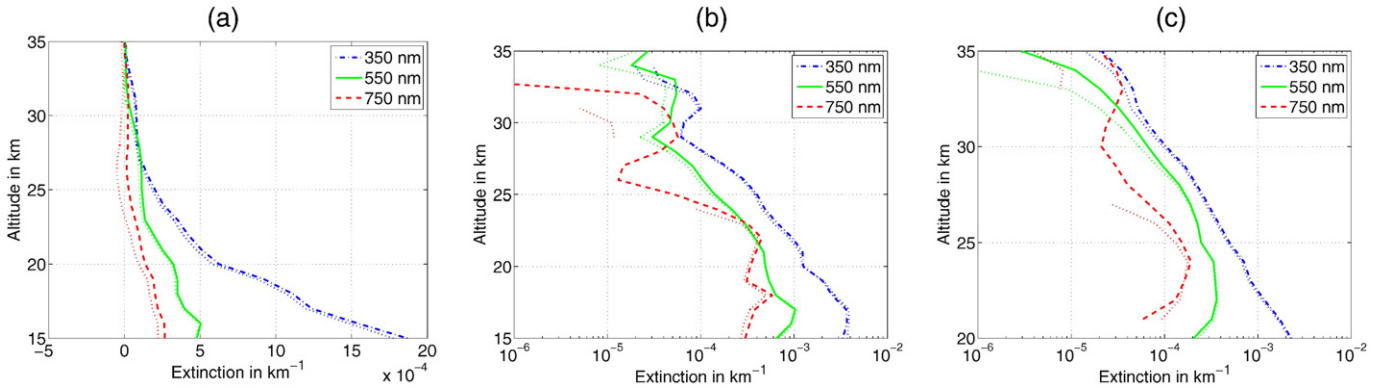

Fig. 1. Examples of vertical aerosol extinction profiles retrieved using the GOMOS cross-section database (dotted lines) and using the revised gas cross-section spectra at 350 nm (blue, dashed-dotted), 550 nm (green, solid) and 750 nm (red, dashed); the date, geolocation and characteristics of the observations shown are specified in Table 2. It has to be noted that the first example is plotted using linear scales; in examples (b) and (c), a logarithmic scale is used for the extinction, and missing points in the square-dashed lines correspond to negative extinction values.

of the absorption cross-section spectra. High-resolution spectra were selected whenever it was possible. The most rigorous approach requires using the high-resolution spectra to calculate the forward spectral model before performing a convolution of the total input signal with the instrument point spread function. However, this approach is very demanding in terms of computer resources, and a common simplification consists of applying the convolution by the point spread function directly on the gas cross-section spectrum. Tests were made to verify that this simplified approach is sufficient, and indeed, they showed overall good results at least up to about 30 km. Hence, it was decided to opt for this faster approach and to use the gas cross-sections spectra at the resolution of the GOMOS spectrometers.

The selection of gas absorption cross-section spectra and the set-up of the revised molecular absorption cross-section database are discussed in Appendix A.

Fig. 1 shows three examples of vertical extinction profiles where the improvement of the aerosol retrieval after revision of the gas cross-sections is visible. The date, geolocation and main features of these three occultation measurements are given in Table 2. These examples illustrate how the revision of the gas cross-section database using more recent data with better temperature coverage, a more extended spectral range, a higher spectral resolution and, in the case of ozone, a maximal consistency, leads to a significant decrease of the number of negative values in the vertical aerosol extinction profile, even in cases where the star properties are less favourable for the aerosol retrieval (more particularly, cool and/or dim stars).

3. Development of gridded aerosol data records for Aerosol_cci

GOMOS and the AerGOM algorithm have been selected to provide stratospheric aerosol datasets in the Aerosol_cci project. The high measurement rate (about a million occultations, of which >455.000 dark limb measurements were successfully inverted over the whole mission) ensures global coverage with a good sampling, and the availability of the extinction spectral dependence enables the retrieval of size information and related parameters.

Table 2
Date, geolocation, and star properties of the observations shown in Fig. 1.

Example	Date	Latitude, longitude	Star magnitude	Star temperature
(a)	January 18, 2005	36°N, 96°E	0.736	7000 K
(b)	May 12, 2011	41°S, 52°W	1.166	9700 K
(c)	February 11, 2006	18°N, 135°E	1.672	10,200 K

Data retrieved with the GOMOS-AerGOM algorithm are used to produce gridded time series (1) to provide datasets to constrain or validate climate models; (2) to characterize the aerosol radiative forcing in the stratosphere; (3) to provide intercomparison datasets for validation of other remote sensing experiments.

In a first step, the inversion of each occultation measurement by AerGOM (Level 2) provides a set of aerosol parameters relevant for the production of CDRs. The main parameter is the vertical extinction coefficient calculated at 5 wavelengths (355, 440, 470, 550, 750 nm) as described in Section 2.2. In their latest version, the CDRs provide also a first version of size information parameters derived from the extinction coefficient, as well as related microphysical and radiative parameters, which will be discussed in a later publication. Table 3 provides an overview of the aerosol parameters derived from GOMOS measurements. All parameters are provided together with their uncertainty. Several additional fields are also included in the CDR, such as the number of observations used in the extinction coefficient and AOD binning, for each point of the latitude, longitude, time and altitude grid.

Before computing the Level 3 gridded dataset from the Level 2 AerGOM data, an observation selection ensures a sufficient quality of the data, based on criteria applied to the star parameters and solar zenith angle of the observations. Since, in the case of GOMOS, there are large differences in data quality related to these parameters, care must be taken to choose the best trade-off between data quality and coverage, two major requirements for the use of the CDRs in climate modelling applications. The choice of selection criteria is discussed later in this section. It should be noted that observations made when the spacecraft was within the Southern Atlantic Anomaly (SAA, anomaly of the Earth's magnetic field) are removed to avoid contamination by noisy measurements.

The CCI-GOMOS CDRs are designed as gridded fields resolving longitude, latitude, altitude and time (Level 3). In the first versions of the CDR, the choice of 2.5° latitude intervals was made to provide a good latitudinal resolution. Considering the number of observations achievable per bin led to the choice of a longitudinal grid resolution of 10° and a monthly averaging. However, User feedback stated that this choice was not optimal to resolve moderate volcanic signatures: the dissipation of the plume during the first days or weeks after the eruption mostly results in lower aerosol concentrations over a large area, which are hardly detectable from the aerosol background. Additionally, taking into account the dominant zonal displacement of the volcanic plumes due to the prevailing winds, the ratio 2.5° latitude/10° longitude/monthly time interval is not well adapted to describe atmospheric motions, nor to cover the typical spread of the plume during one grid time interval. Therefore, in later versions, the grid cell was revised to an optimized choice of 5° latitude by 60° longitude by 5 days. This choice is more suitable to describe the zonal aerosol distribution. With respect

Table 3
List of stratospheric aerosol parameters provided by Aerosol_cci.

Parameter	Unit	Data source	Calculation from occultation measurement	Comment
Vertical extinction profile	km^{-1}	GOMOS residual extinction coefficient (transmissions corrected for refractive effects)	See Section 2.2	At 355, 440, 470, 550, 750 nm Provided for the total aerosol extinction coefficient (all aerosol types included), sulfate aerosol fraction and PSC
AOD	–	Vertical extinction coefficient	Integration of the extinction coefficient down to 2 km above tropopause	
Ångström exponent	–	Extinction coefficient at the different wavelengths	Regression over the spectral dependence	

to the latitudinal and temporal resolution, it also complies better with the most critical CGOS requirement for the stratospheric aerosol extinction coefficients (given in Table 1) of about 200–500 km horizontal (1 degree ~110 km) and weekly temporal resolution, while the weaker longitudinal resolution is not as critical given the typical zonal transport. Typically, up to 20 observations are available per grid cell, depending on the location of the satellite and on the stars available. The number of observations is provided as additional field in the CCI-GOMOS dataset.

Binning is performed on each grid cell using only quality-filtered data, and the variability is estimated for each bin from the spread of the measurement samples. The criteria used for the filtering, which are discussed in Section 4, concern the star selection and the solar zenith angle (SZA), the main factors influencing the signal-to-noise ratio (SNR). In order to maximize the number of data used to compute the binned values while not being too sensitive to outliers, we use a weighted average of all values comprised between percentiles 10 and 90. However, if <10 points are available in the bin sample, all the values are used for the averaging. So far, the uncertainty on each bin is computed as the average of all uncertainties between percentiles 25 and 75 (interquartile mean, IQM). This representation of the typical measurement uncertainty seems more realistic than the error of the mean, because it excludes outliers as can be found more particularly from occultations with a poor SNR (See Section 3.1).

Obviously, the primary factors influencing the quality of the CCI-GOMOS CDRs are the performance of the AerGOM retrieval algorithm and the amount of data available for binning. The very first task was hence to assess the performances of the retrieval algorithm and the outcome of this study can be found in Robert et al. (2016). Several improvements of the AerGOM implementation led to a significant increase of the data quality, which had two positive consequences: (1) an increase of the number of observations improving the data coverage, and (2) the possibility to relax the observation selection criteria. In the rest of this section, we show how improvements of AerGOM and a careful selection of the AerGOM dataset led to the maturation of the CCI-GOMOS CDRs.

3.1. Star properties

The early evaluation of the AerGOM algorithm showed the strong influence of star properties on the data quality. Both the temperature of the star (controlling the spectral range of its emission) and its magnitude (quantifying the overall brightness of the star) have an impact on the signal-to-noise ratio, and therefore, on the extinction uncertainty.

In order to assess the exact impact of the star's properties on the quality of the retrieval and on the subsequent observation selection, the extinction uncertainty was studied for several classes of stars. In this paper, we restrict ourselves to the limiting cases of stars (brightest/dimmest; coolest/hottest), which are the most important for the choice of selection criteria. An exhaustive discussion of this study can be found in Robert et al. (2016).

We consider here four classes of stars used by GOMOS. The criteria defining the four star classes in terms of magnitude (bright and dim stars) and temperature (cool and hot stars) are given in Table 4, as well as the typical range of uncertainties found for the extinction coefficient at 550 nm in these specific star classes.

Fig. 2 shows the averaged extinction uncertainty found for the different star classes. The right panel shows the averaged uncertainty as a function of the wavelength and the altitude, and the left panel shows the probability distribution of the uncertainty. For each case, 1000 observations were taken into account to derive the mean values and the probability distributions. From this figure, it appears that the star's magnitude is the main factor influencing the uncertainty: the dim star classes show an uncertainty exceeding in most cases 30% on average, and about 50% outside the 15–25 km altitude range, while for bright stars, typical uncertainties are below 20% in the 15–25 km altitude in the 350–750 nm spectral range. Still, the influence of the star temperature is visible, mainly in the displacement of the uncertainty minimum toward lower (higher) wavelength values for the hot (cool) star classes, which correspond to the spectral range where the stellar emission is maximal. For cool stars, the uncertainty increases below 700 nm and at altitudes outside the 15–30 km range, i.e. where the transmitted signal is typically very faint. The impact of the star properties on the selection criteria is discussed in Section 3.1.

3.2. Solar zenith angle

Another parameter having a strong influence on the data quality is the solar zenith angle (SZA). This angle is provided with a flag indicating the type of illumination conditions (Bertaux et al., 2010). While dark limb conditions with the satellite far enough from the solar terminator ensure good measurement conditions, both internal and external stray light may affect the quality of the measurement when the satellite is close to the terminator. The effect of stray light is corrected during the processing of the GOMOS Level 1 dataset, but it is likely that residual signatures of stray light remain, increasing the uncertainty of the retrieval.

The range of SZA values, which depends on the position of the satellite along its orbit, is not equally distributed over the latitude range. Low values of the SZA characterize higher latitude observations, while the occultations at central latitudes correspond to the highest values of the SZA (Fig. 3). Hence, any selection criteria applied to the solar zenith angle to ensure a good data quality has an impact on the data coverage,

Table 4
Definition of the star classes used to study the influence of star properties on the quality of the extinction coefficient.

Star class	Magnitude	Temperature	Typical extinction uncertainty at 550 nm
Bright – Cool	−1.5 to 1.5	2800 to 5600 K	15–30%
Bright – Hot	−1.5 to 1.5	26,000 to 39,000 K	5–15%
Dim – Cool	2.6 to 3.0	2800 to 5600 K	40–70%
Dim - Hot	2.6 to 3.0	26,000 to 39,000 K	30–60%

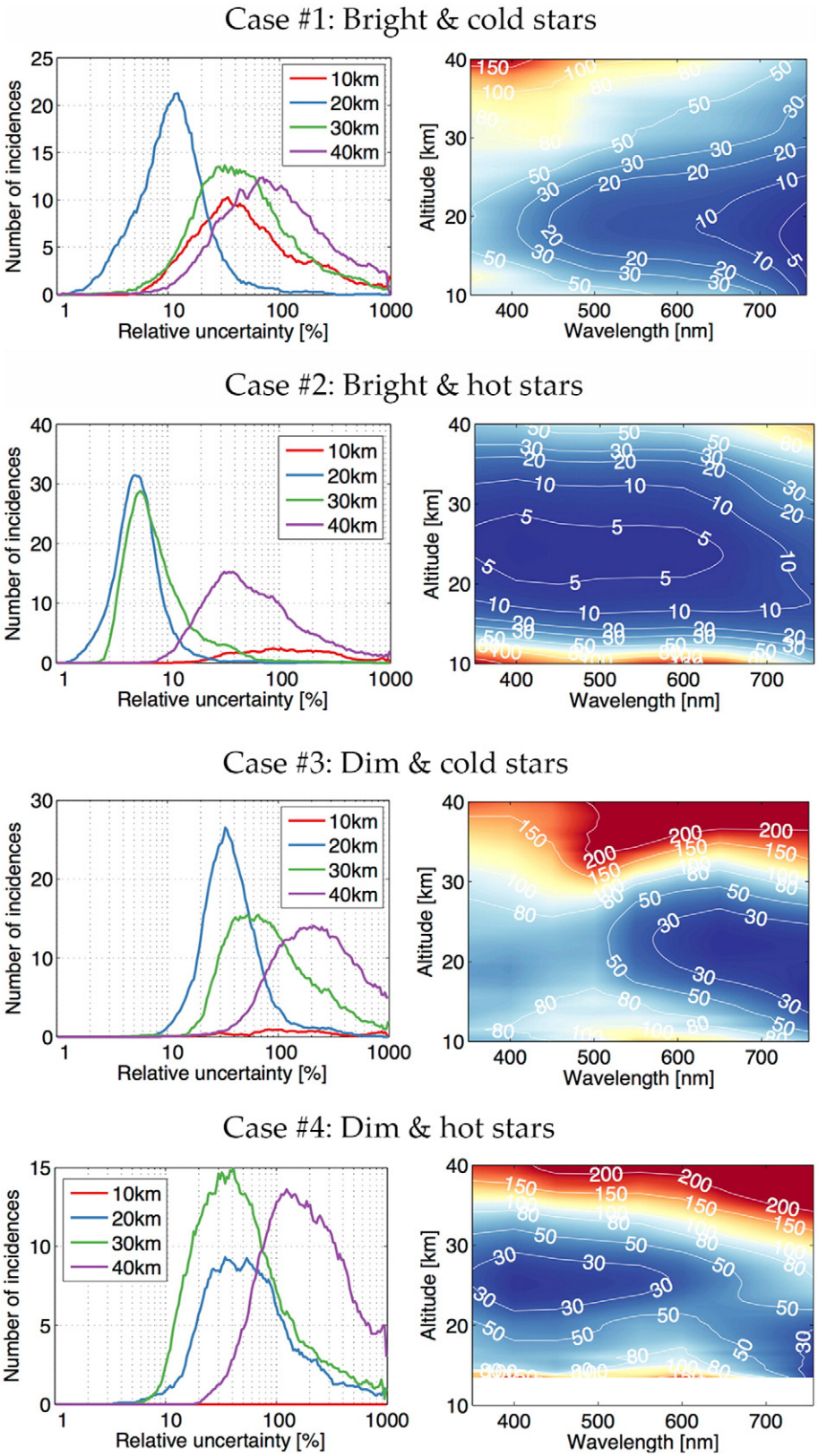

Fig. 2. Extinction coefficient uncertainty for different star classes: (1) Bright and cool stars; (2) Bright and hot stars; (3) Dim and cool stars; (4) Dim and hot stars. In each case: left panel: uncertainty probability distribution at 10 km (red), 20 km (blue), 30 km (green), and 40 km (purple) altitude and at 550 nm. Right panel: contour plots of the mean relative uncertainty of the aerosol extinction coefficient as a function of altitude and wavelength.

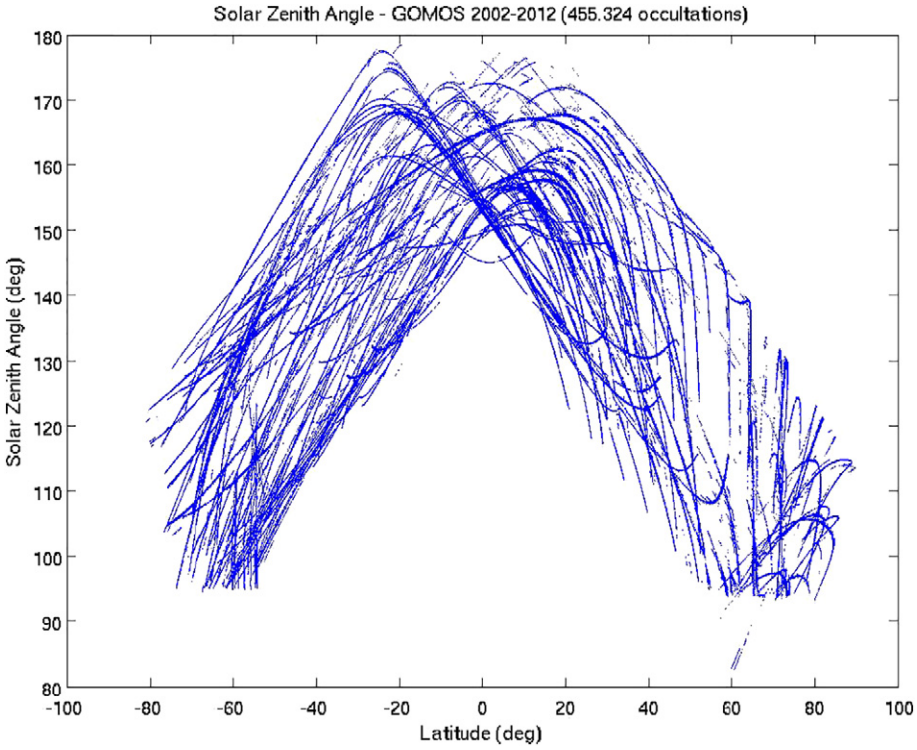

Fig. 3. Latitudinal distribution of the occultation solar zenith angle during the whole GOMOS mission. Each point represents one occultation, indicated by its latitude and corresponding SZA.

decreasing the coverage at high latitudes. Consequently, the SZA is a determining parameter to choose the trade-off between maximum coverage and maximal data quality.

In the first CCI-GOMOS version, conservative values of the minimum SZA were used. Afterward, although Robert et al. (2016) recommend to use single AerGOM occultations only if SZA > 130° at long wavelengths (~700–750 nm), the use of a binning allowed for less restrictive selection criteria on the SZA. Relying on the successive improvements of AerGOM, and more particularly the resolution of the problem of anomalous profiles discussed in Section 2.3, the selection criteria could be gradually relaxed, resulting finally in the criterion SZA > 100 used in the latest version of the CCI-GOMOS CDR.

4. Aerosol_cci stratospheric data records

Taking advantage of the successive improvements, of which the main ones were discussed in the previous section, different versions of the CCI-GOMOS CDR were developed, first for the reference year 2008, and later for the whole GOMOS dataset. Table 5 reports the features of the main versions produced for the CCI-GOMOS CDR spanning the whole ENVISAT period. This overview shows the gradual relaxation of the selection criteria reflecting the improvements discussed in the previous section. The transition from version 2.14 to 2.19 corresponds to the User's recommendation to adapt the grid and time resolutions to provide a more useful picture of the evolution of volcanic plumes. Version 3.00 benefits mainly from the consolidation of the code, and provides several additional aerosol fields such as extinction coefficient at five wavelengths commonly used in other space-borne or ground-based instruments, but also size information and related parameters which are not within the scope of this paper.

As an illustration, the CCI-GOMOS time series of aerosol extinction coefficient at 550 nm and 17 km for the whole ENVISAT period (2002–2012) is shown in Fig. 4. For comparison, the time series for both versions 3.00 (upper panel) and 2.19 (lower panel) are shown. As discussed in Section 3.2, version 3.00 shows a better coverage at high latitudes than version 2.19. In both cases, an overall increase of aerosol burden marked by enhanced values of the aerosol extinction coefficient is clearly visible until about 2008. Both time series also show the contribution from large equatorial volcanic eruptions such as Soufriere Hills (16°N, 62°W) in May 2006 and Rabaul (4°S, 150°E) in

Table 5
Main specifications of the most prominent versions of the CCI-GOMOS CDR (Level 3).

CCI-GOMOS and related (AerGOM) version	Selection criteria	Spatial resolution	Temporal resolution	Extinction wavelength provided (nm)
2.14 (AerGom 2.0)	Star magnitude < 2.6 Dark limb only No SAA profiles Star temperature > 5000 K	2.5° latitude 10° longitude 1 km vertical	1 month	550
2.19 (AerGom 2.0)	Star magnitude < 2.6 SZA > 105° No SAA profiles Star temperature > 5000 K	5° latitude 60° longitude 1 km vertical	5 days	550
3.00 (AerGom 3.0)	Star magnitude < 3 SZA > 100° No SAA profiles Star temperature ≥ 2800 K	5° latitude 60° longitude 1 km vertical	5 days	355, 440, 470, 550, 750

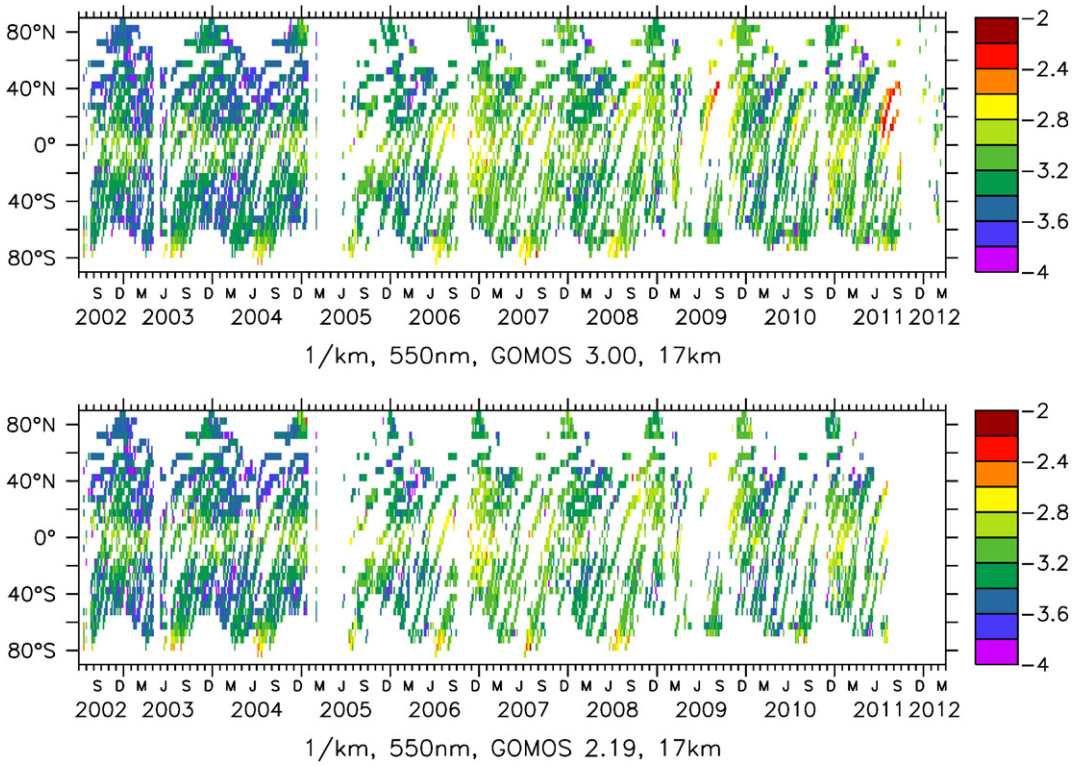

Fig. 4. Aerosol extinction coefficient at 550 nm and 17 km altitude for the time-period 2002–2012 (decadal logarithm). Upper panel: CCI-GOMOS CDR, version 3.00 (Level 3); Lower panel: same, from version 2.19.

October 2006 (Brühl et al., 2015), although few data are available in Fall 2006 at such low altitude, as compared to higher altitudes. The eruptions of Kasatochi (52°N, 175°W) in August 2008 and Sarychev (48°N, 153°W) in June 2009 were hardly observed by GOMOS because, due the orbital characteristics and star availability, almost no measurements were made above 50°N in this period (See, for instance, Fig. 9 in Bertaux et al. (2010)). Nevertheless, the signature of the plume could still be observed in Fall 2008 at mid-latitudes in the northern hemisphere.

Fig. 4 demonstrates the improvement of the coverage between versions 2.19 and 3.00. A particularly clear illustration concerns the volcanic signatures of the Sarychev (48°N, 153°W) plume immediately after the eruption in June 2009, and of the Nabro (13°N, 42°E) eruption in June 2011, which injected a huge amount of ash and sulfurous gas into the stratosphere (about 496 and 446 kt SO_2 respectively, see Table 7), the latter being converted to stratospheric aerosols and detected by instruments such as GOMOS. These signatures are hardly visible in the version 2.19 data time series despite the strength of the emissions, due to a lack of data points. In version 3.00, the amount of observations taken into account in the binning is much larger due to the relaxation of the selection criteria, and the increased data coverage is now sufficient to resolve these additional signatures. The use of this improved time series will be discussed in more detail in Section 6, and illustrated in Appendix C.

5. Validation

The validation of the AerGOM (version 3.0) and CCI-GOMOS extinction datasets has been the subject of various activities, in and outside the Aerosol_cci project. Robert et al. (2016) performed extensive intercomparisons of the AerGOM dataset with several other satellite measurement datasets such as SAGE (Stratospheric Aerosol and Gas Experiment) 2 and 3, POAM (Polar Ozone and Aerosol Measurement), ACE-MAESTRO (Atmospheric Chemistry Experiment/Measurements of Aerosol Extinction in the Stratosphere and Troposphere Retrieved by Occultation), OSIRIS (Optical, Spectroscopic, and Infrared Remote Imaging System), and GOMOS-IPF. Recently, the CCI-GOMOS dataset also participated to the assessment of trace gases and aerosols in the framework of the SPARC Data Initiative (SPARC, 2017). Intercomparisons included the same datasets, as well as SCIAMACHY. A paper on the SPARC Data Initiative assessment is currently in preparation (Hegglin et al., to be published in J. Geophys. Res.) and this work will not be described here. Finally, the Aerosol_cci Validation Team of the project conducted intercomparisons using ground-based and spaceborne lidars. Although comparisons are more difficult between lidars and a dataset such as AerGOM because the quantities measured by both instruments are different, the interest of these intercomparisons resides in the fact that lidars provide time series of measurements with a very good temporal frequency and a high vertical resolution; they don't present the same kind of limitations or aging characteristics as spaceborne occultation of limb scattering measurements. Therefore, they can provide very valuable information on the quality and stability of GOMOS.

Lidars operated routinely or for long-term time periods to perform stratospheric aerosol measurements provide high-resolution vertical backscatter profiles only. Therefore, the validation cannot be performed in the strictest sense, as the global extinction-to-backscatter ratio (E/B) is not known (future satellite lidar missions like ADM-Aeolus will measure this quantity). The CCI-GOMOS extinction time series has been evaluated using stratospheric aerosol lidar measurements provided by three different ground-based stations, which are parts of the Network for the Detection of Atmospheric Composition Change (NDACC) network (e.g. Steinbrecht et al. (1997)). Validating a gridded extinction profile from global remote observations using lidar profiles is not an easy task: both kinds of observations measure different physical quantities, are affected by specific sources of error, are characterized by different vertical resolutions and reflect different realities (averaged extinction coefficient of the corresponding grid cell in one case, local instantaneous measurement in the other). Therefore, it was decided to first validate extinction profiles from individual AerGOM measurements (Level 2), which are not subject to statistical effects. Then, we validated the CCI-GOMOS extinction time series (Level 3) giving some mean estimate representative for the considered bin, in a second step. In addition

to these two validation exercises, we present a comparison with CALIOP zonal mean extinction coefficient for the year 2008.

5.1. The NDACC stratospheric aerosol lidar data

Since the 1970s ground-based observations of stratospheric aerosols have been performed within NDACC. Quality assurance of the data is guaranteed through instrumental and analysis inter-comparisons (e.g. Steinbrecht et al., 1997). For the time frame when GOMOS measurements are available, i.e. between April 2002 and April 2012, we chose three NDACC lidar stations representative for different latitude ranges: Garmisch Partenkirchen (Germany) (Jäger, 2005; Trickl et al., 2013), a lidar station at northern mid-latitudes; Mauna Loa (Hawai, USA) (Barnes and Hofmann, 1997, 2001; Antuña et al., 2003; Hofmann et al., 2009), a northern hemisphere sub-tropical site; and Dumont D'Urville, situated in Antarctica (Chazette et al., 1995; David et al., 2012). An overview of these lidar stations and the corresponding dataset available for validation is given in Table 6.

If not given as primary product, the aerosol backscatter coefficient β^{aer} at wavelength $\lambda = 532$ nm and altitude z has been calculated from the backscatter ratio BSR and the molecular backscatter coefficient β^{ray} as follows:

$$\beta^{aer}(z) = (BSR - 1) \times \beta^{ray}(z) \tag{4a}$$

or

$$BSR(\lambda, z) = \left(\beta^{aer}(z) + \beta^{ray}(z)\right) / \left(\beta^{ray}(z)\right) \tag{4b}$$

The molecular backscatter coefficient β^{ray} can be calculated using the ideal gas law from the altitude dependent molecular number density N(z) or the atmospheric temperature T(z) and pressure profile P(z) and the differential Rayleigh backscatter cross section $(d\sigma^{ray}(\pi)) / d\Omega$:

$$\begin{aligned}\beta^{ray}(z) &= N(z) \times \left(d\sigma^{ray}(\pi)\right)/d\Omega. \\ &= (N_A * P(z))/(R_a * T(z)) \times \\ &\quad \left(d\sigma^{ray}(\pi)\right)/d\Omega\end{aligned} \tag{5}$$

where the value π reflects the fact that the scattering angle is equal to 180 degrees, Ω is the solid angle for detection, N_A, the Avogadro constant and R_a, the gas constant for dry air. The Rayleigh backscatter cross-section for wavelength λ can be approximated as (Collis and Russell, 1976):

$$d\sigma^{ray}(\lambda)/d\Omega = 5.45 \times (\lambda/(550))^{-4.09} \times 10^{-28} \left(cm^2\ sr^{-1}\right) \tag{6}$$

Finally, the aerosol extinction coefficient α^{aer} is calculated using the reported values or a pre-defined extinction to backscatter ratio E/B:

$$\alpha^{aer}(z) = E/B(z) \times \beta^{aer}(z) \tag{7}$$

The largest caveat of the comparison is the uncertainty related to the unknown extinction-to-backscatter ratio. Therefore, the other uncertainties related to the NDACC lidar measurements were not taken into account.

The aerosol E/B for stratospheric background aerosol, non-absorbing sulfur acid droplets with known refractive index, can be approximated using Mie calculations (e.g. Rosen and Hofmann, 1986). Values between 30 sr and 60 sr were observed for background conditions and after major volcanic eruptions respectively (e.g. Jäger et al., 1995, Chazette et al., 1995, Jäger and Deshler, 2002). For Polar stratospheric clouds (PSCs), E/B can vary depending on the PSC type. For PSC type I and II (PSC type II being ice PSCs) Reichardt et al. (2004) report E/B values between 56 and 135, and between 16 and 42, respectively. Several authors report E/B values for ice PSCs and cirrus clouds around 20 (e.g. Chen et al., 2002, Noel et al., 2009).

For the comparison between GOMOS and the NDACC lidar we chose E/B = 50 sr as representative for stratospheric background conditions, unless a time and altitude dependent value was provided in the NDACC dataset, like in the case of Garmisch-Partenkirchen. For that site E/B varies between 40 sr and 50 sr in the stratosphere and between 10 and 70 sr between 5 and 14 km altitude. Additional statistics for E/B between 30 (large volcanic influence) and 70 sr are given in Appendix B.

5.2. Validation of Level 2 extinction coefficient at 550 nm

First, the AerGOM level 2 (L2) data, version 3.0 have been compared to the NDACC lidar data. A spatial difference of 500 km and a temporal difference of 12 h have been used as co-location criteria. An example comparison is given in Fig. 5, showing the AerGOM data (blue) and the lidar profiles (red). The profiles from the Mauna Loa observatory on 13 November 2008 show the increased aerosol layer remaining from the eruption of the Kasatochi volcano (52°N, 176°W) in August 2008 (Wang et al., 2013). For the comparison, the lidar data have been smoothed when the altitude resolution was finer than 100 m, and interpolated to the AerGOM vertical grid. Further, the interpolated lidar profiles have been convolved with the AerGOM averaging kernel (shown on the left panel) and compared to the AerGOM profiles.

A statistical analysis has then been carried out for each of the three reference datasets (Garmisch-Partenkirchen, Mauna Loa and Dumont d'Urville) on a one-kilometer altitude grid. This analysis has been performed for E/B values of 30, 50 and 70 sr taking into account the observation selection criteria used in versions 2.19, 3.00 and for a "best case" defined as a test selection assuming very conservative selection criteria: star magnitude < 2, solar zenith angle > 105°, and star temperature > 5000 K. Selection criteria for versions 2.19 and 3.00 are given in Table 5. In the case of Garmisch-Partenkirchen, however, instead of the fixed value E/B = 50, we have used the E/B value given in the NDACC lidar dataset. In addition, a separate statistical analysis was performed for PSC observations, as identified by the AerGOM aerosol type flag using the temperature criterion $T < 197$ K. This last PSC validation was applied to the Dumont d'Urville dataset, the only one concerning the polar regions. The aim of this analysis using three different values of E/B is to take into account the possibility that the standard value of 50 sr is not optimal to describe specific aerosol types or altitude/latitude ranges. Performing the same statistical analysis for both CCI-GOMOS versions 2.19 and 3.00 is important to verify that the relaxation of the observation selection criteria (specified in Table 5) does not alter the accuracy of the extinction time series. A detailed presentation of this extended evaluation of the CCI-GOMOS CDRs is given in Appendix B.

Table 6
Overview of NDACC lidar sites providing reference datasets. The indicated available period is restricted to the period of interest for this work (April 2002–April 2012) and is given as month/year. The used parameters are indicated as follows: BSR: backscatter ratio, T: temperature, P: Pressure, $\log_{10}$N: $\log_{10}$ of molecular number density, E/B: extinction-to-backscatter ratio, β^{aer}: aerosol backscatter coefficient.

Location	Latitude, longitude	Available period	Provided parameters	Number of month (M) and profiles (P) available	Reference altitude (indicative; in km)
Garmisch – Partenkirchen, Germany	47.5°N, 11.1°E	01/2003–11/2010	β^{aer}, E/B	M: 79, P: 236	30–40
Mauna Loa, Hawaii, USA	19.5°N, 155.6°W	02/2004–04/2012	BSR, $\log_{10}$N	M: 121, P: 409	35–40
Dumont d'Urville, Antarctica	66.7°S, 140.0°E	06/2006–04/2012	BSR, T, P	M: 44, P: 380	28–32

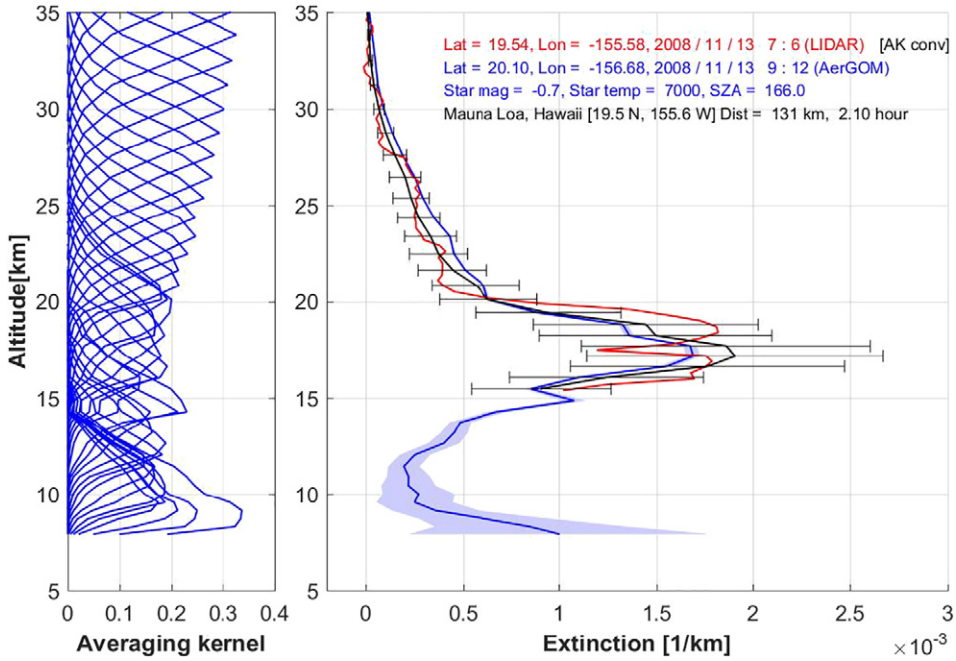

Fig. 5. Example of comparison between AerGOM and lidar profiles from Mauna Loa observatory. Left panel: the AerGOM averaging kernel. Right panel: the AerGOM profile (in blue), blue region: AerGOM uncertainty, the lidar data (red line), and the lidar data convolved with AerGOM averaging kernel (black). The black error bars on the lidar data show the variations when using E/B of 30 sr and 70 sr instead of 50 sr.

Fig. 6 shows an overview of the statistical analyses performed using the 3 reference lidar datasets, with in the case of the Dumont d'Urville lidar station, separate analyses for liquid sulfate aerosols and PSCs as identified by the AerGOM aerosol type flag. In all four cases, two different statistical analyses are conducted using the CCI-GOMOS version 3.00. The plots on the left hand side show a statistical analysis taking into account all AerGOM profiles relevant for the considered case. The AerGOM median and the spread of the distribution defined as an interval of two times the standard deviation centered on the median, are shown by the blue curve and the light blue region, respectively. The same quantities are plotted as black solid lines and error bars for the lidar measurements. Relative standard deviation are also plotted on the central panel for comparison with the relative difference between AerGOM and the lidar dataset (in green). This analysis shows that, for all four cases considered, AerGOM version 3.0 and the lidar dataset agree within the spread of the distribution. It should be noted that, due to the fact that version 3.0 used here is processed with the most relaxed event selection criteria (See Table 5), the agreement is even better in the case of versions 2.19 (not shown here).

Although these results look satisfactory, it is worth mentioning that the statistical sampling considered in this first analysis includes outliers which enlarge the error bars and makes this analysis of limited interest. Therefore, another statistical analysis was made, restricting the AerGOM sampling by rejecting outliers. This analysis is illustrated on plots at the right hand side of each panel. In these cases, outliers are, defined as all values lying out of 1.5 times the interquartile range (IQR), where the IQR is the range defined by the interval between percentiles 25 and 75 of the statistical sampling. The plot shows the IQM (red line) and the IQR (rectangular box). The dashed lines show the range of values which are not considered as outliers, and the red crosses show, for each case, individual outliers encountered in the AerGOM data sampling.

For this second statistical analysis, all cases show agreement between both AerGOM and lidar datasets, except in the case of Garmisch-Partenkirchen, where the Level 2 profile comparison shows a bias at all altitudes, and agreement within the IQR only below 19 km. AerGOM values are higher on average, which can indicate the presence of a real bias, an underestimation of the E/B for the lidar profile conversion, or a combination of both factors. Both datasets agree within the error bars, representing two times the standard deviation. The lidar station at the Mauna Loa observatory provides data down to 15 km altitude. For this station, the individual comparisons between AerGOM and lidar profiles show many observations with similar profiles and in general the agreement between individual co-located profiles is good and within the uncertainties. Also observations from Dumont D'Urville lead to a good overall agreement.

Some individual PSC extinction profiles show a clear disagreement with particularly large lidar values compared to the AerGOM data (not shown here), which may correspond to ice PSCs characterized by an E/B value of about 25. We expect to obtain a better statistical agreement by analyzing separately PSCs of different types, which are expected to correspond to different values of E/B. This will be the subject of future validation work.

Another reason for disagreement between AerGOM and lidar vertical extinction profiles might be the spatial distance and time between both observations, and the different viewing conditions which lead to observing a local and rapidly evolving pattern such as a PSC by one instrument, or by both instruments at different stages of their evolution. Illustrations of this phenomenon are shown in Section 5.3.

5.3. Validation of Level 3 extinction coefficient at 550 nm

The evaluation of the GOMOS level 3 dataset was applied to CCI-GOMOS CDRs in versions 2.19 and 3.00, of which the characteristics are given in Table 5. Lidar profiles were selected within the bin spread (time period of 5 days, latitude and longitude intervals of 5° and 60° respectively).

Fig. 7a,b illustrates the statistical analysis of Level 3 comparisons for the CCI-GOMOS extinction dataset in version 2.19 and 3.00. For Garmisch-Partenkirchen, the agreement improves with respect to the Level 2 intercomparisons: the variability in L3 is integrated within a bin cell, making it closer to the lidar profiles on average. This averaging is particularly effective in case of rapidly evolving structures, such as PSCs. Level 3 intercomparisons for Mauna Loa give quite similar results

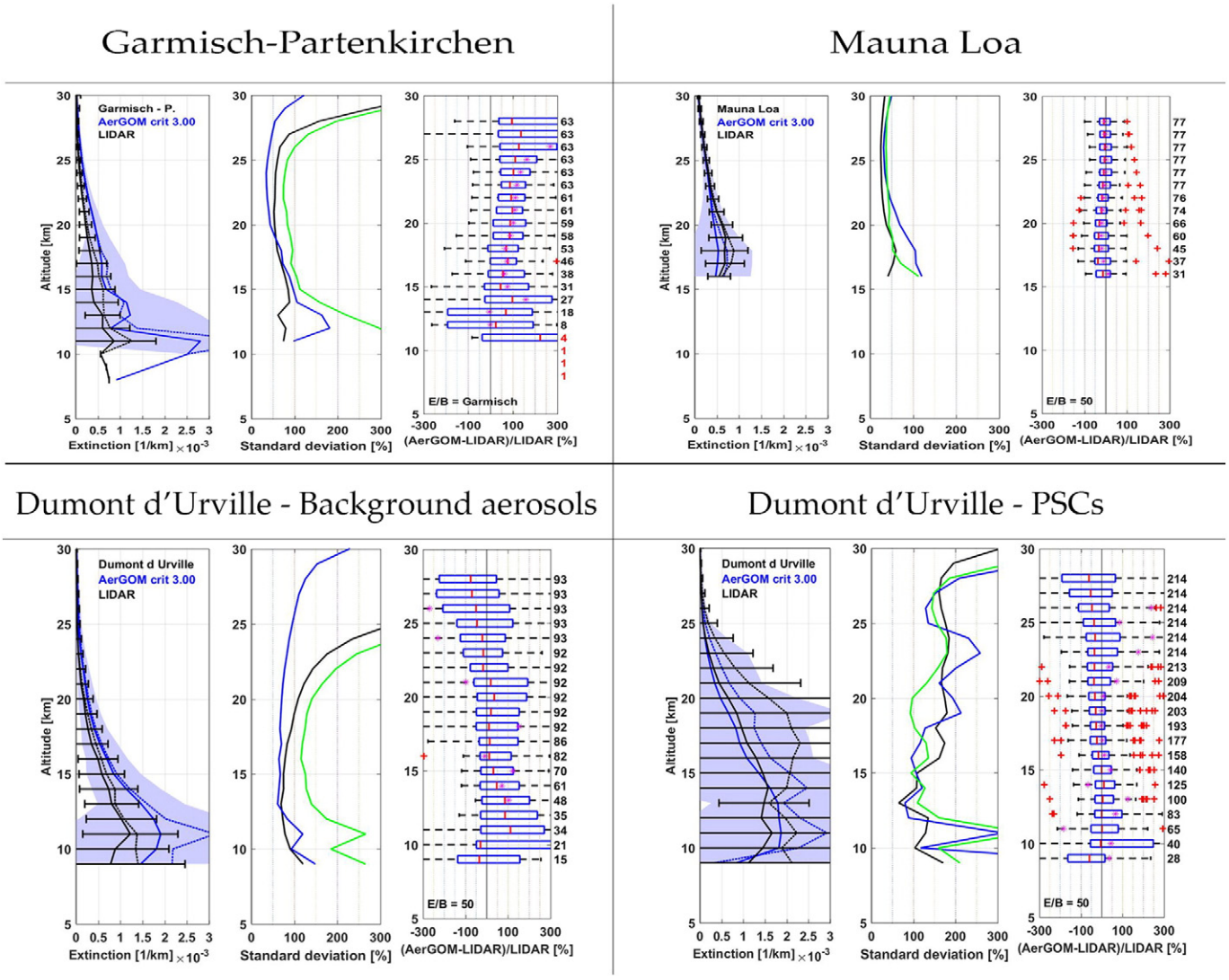

Fig. 6. Comparison between AerGOM level 2 ("GOMOS", in blue) and lidar profiles (black) for Garmisch Partenkirchen (upper left panels), Mauna Loa observatory (upper right panels) and Dumont D'Urville identified as background aerosol (lower left panels), and as observations affected by PSC influence (lower right panels). See explanation in the text for the description of the different plots. For each station: plot at the left hand side (co-located datasets): blue solid and dotted lines: median and mean of AerGOM dataset, respectively; blue region: 2-sigma interval across the AerGOM median value; black solid and dotted lines: median and mean of lidar dataset, respectively; error bars: 2-sigma interval across the lidar values. Central plot: blue line: relative standard deviation of AerGOM data; black line: relative standard deviation of lidar data; green line: relative standard deviation of the difference between the AerGOM and lidar data, relative to lidar data. Plot at the right hand side: red vertical lines and magenta stars: IQM and median of the relative differences between AerGOM and lidar co-located events (in %); rectangular box: interquartile range; dashed lines show the range of valid values of the relative difference; red crosses show individual occurrences of outliers, as defined in the text. The numbers of co-located data, which have been found in the respective altitude bins, are given on the right y-axis. In each case, the E/B value is indicated in the bottom left-hand corner. In the case of Garmisch, "E/B = Garmisch" means that the used E/B values are the ones provided in the lidar dataset.

as for the Level 2 evaluation. In this case where no particular rapidly evolving patterns are expected in the background aerosol layer, the averaging does not bring additional statistical benefit from integration. Finally, for the lidar station at Dumont D'Urville, the statistical analysis on the Level 3 extinction dataset includes all cases, covering background sulfate aerosol and PSCs. Both AerGOM and lidar datasets agree well within the uncertainties.

Fig. 8 shows a time series of PSC observations made at Dumont D'Urville in the 5-day CCI-GOMOS time interval 12–17 September 2007. For this time interval, four co-located lidar profiles were found, and compared to the same CCI-GOMOS binned extinction profile. Lidar data are shown in black, while the CCI-GOMOS data in versions 3.00 and 2.19 are coloured in magenta and blue, respectively. The PSC observed by the lidar is growing throughout the time period covered by this 5-day CCI-GOMOS grid cell, and the agreement is best for version 3.00 in the latest co-location shown. This example illustrates the effect of sampling in the GOMOS dataset in case of a rapidly evolving dynamical pattern, which should be taken into consideration when interpreting the validation statistics presented here.

Fig. 7. Statistics for comparison between CCI-GOMOS version 2.19 and 3.00 and NDACC lidar profiles for Garmisch-Partenkirchen (upper panel), and Mauna Loa observatory (lower panel). For each station: First panel (co-located datasets): median (solid) and mean (dashed) values of CCI-GOMOS versions 2.19 (red) and 3.00 (blue), respectively; magenta and blue regions: 2-sigma interval across the AerGOM median value, for versions 2.19 and 3.00, respectively; black solid and dashed curve: median and median of lidar dataset, respectively; error bars: 2-sigma interval across the lidar values. Second panel: blue and magenta line: relative standard deviation of GOMOS data version 2.19 and 3.00; black line: relative standard deviation of lidar data; green and cyan line: relative standard deviation of the difference between the GOMOS data version 2.19 and 3.00 and lidar data, relative to lidar data. Two last panels: The two whisker plots show median (red vertical lines), inter-quartile range (left and right edge of the boxes) for the relative differences between the GOMOS versions 2.19 and 3.00 and lidar data [in %]. The whiskers extend to the most extreme data points not considered outliers, and outliers are plotted individually using red crosses.

Garmisch-Partenkirchen

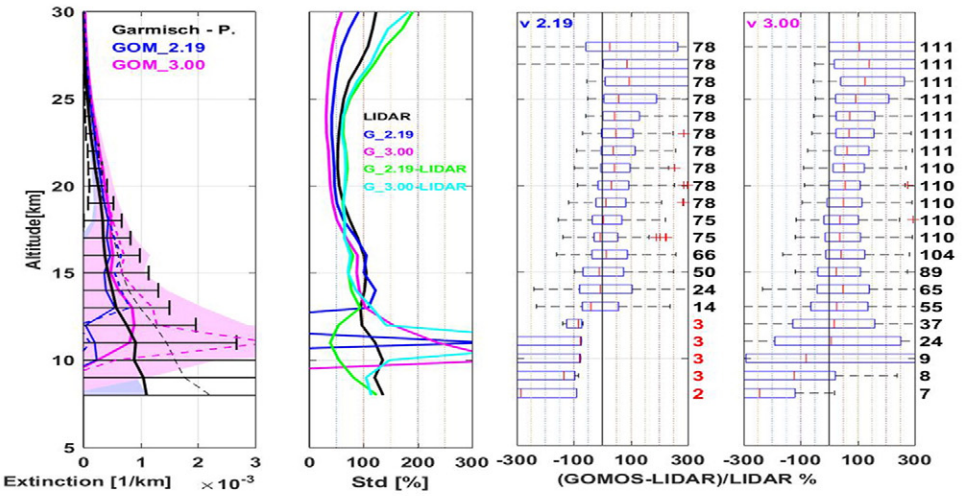

Mauna Loa

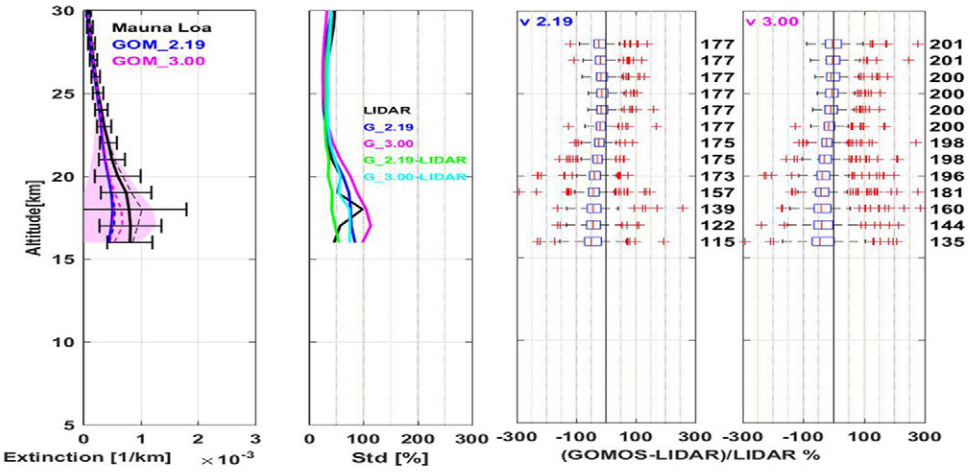

Dumont d'Urville

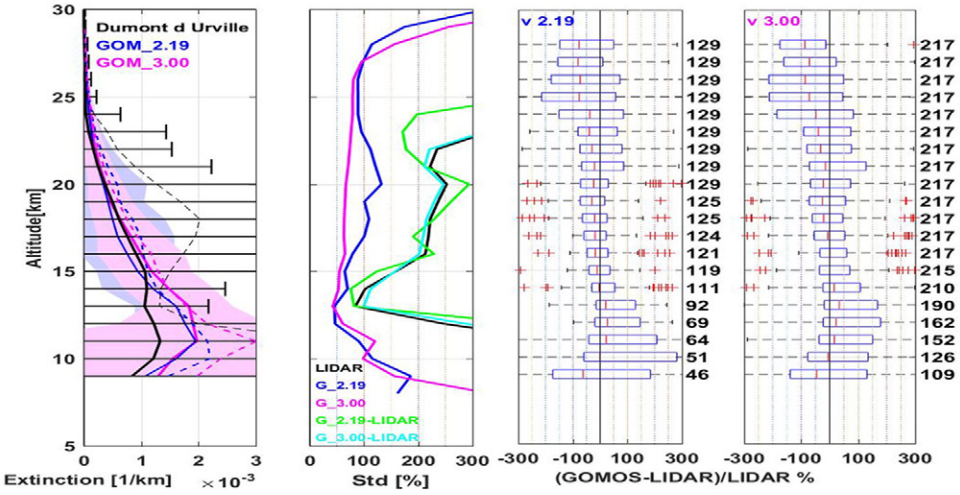

5.4. Comparison of CCI-GOMOS and CALIOP stratospheric aerosol extinction coefficient at 550 nm in 2008

Since June 2006 the Cloud-Aerosol Lidar with Orthogonal Polarization (CALIOP) on board Cloud-Aerosol Lidar and Infrared Pathfinder Satellite Observations (CALIPSO) is monitoring aerosols and clouds in the atmosphere. CALIOP is a lidar instrument measuring backscatter profiles at 532 nm and 1064 nm, as well as the depolarization at 532 nm with a vertical resolution of 60 m and 300 m within the altitude ranges 8.2–20.2 km and 30.1–40 km, respectively. CALIPSO is part of the A-Train and evolves in a polar orbit providing measurements at 01:30 and 13:30 local time (Winker et al., 2009).

A specific treatment of the CALIOP level 1 V3.01 product was applied to retrieve stratospheric aerosol backscatter and extinction profiles. The CALIOP dataset were grouped into 16-days periods and the total attenuated backscatter and depolarization ratio profiles was averaged over 1-degree intervals along the orbit track. Correction of the transmission for molecular scattering and ozone absorption was applied. The molecular backscatter is retrieved using air density from GMAO (Global Monitoring and Assimilation Office) data reanalysis and removed from the total backscatter measured by CALIOP to retrieve the aerosol backscatter coefficient. In order to correct a known calibration bias, the data have been recalibrated between 36 and 39 km, which is a cleaner region of the stratosphere compared to the 30–34 km altitude range used operationally. The treatment of the CALIOP level 1 data in the stratosphere can be found in (Vernier et al., 2009). For the purpose of the comparison with CCI-GOMOS, the data have been regrouped into bins of 1° latitude × 10° longitude × 0.2 km and a fixed E/B value of 50 sr has been used for the conversion of CALIOP backscatter into extinction coefficient.

In Fig. 9, we show the latitude/altitude dependence of the extinction coefficient derived from CALIOP (left panel) and the corresponding extinction coefficient from the CCI-GOMOS CDR (version 3.00, middle panel) for two periods. The first period covers a stratospheric background-period (January–April 2008) while the other one spans the end of the year (here September–December), where the eruption of the Kasatochi volcano (52°N, 176°W) in August 2008 led to an increase of stratospheric aerosol over the northern hemisphere (Wang et al., 2013). This is well captured by GOMOS and CALIOP (see Fig. 9, lower panels). Using a fixed lidar ratio of 50 sr, typical for stratospheric background sulfate aerosols, the CCI-GOMOS data are underestimated with respect to CALIOP. This mismatch can be due to a negative bias of GOMOS with respect to CALIOP, or to a bad choice of the E/B value to convert CALIOP backscatter into extinction profiles.

This latter hypothesis was tested by recomputing E/B from CCI-GOMOS extinction coefficient values and the CALIOP backscatter profiles for the same latitude/altitude region. The result of this test is given in Fig. 9, right panels. For both time periods, similar values of the reconstructed E/B are found over large regions, and on the other hand, a large range of E/B is observed on the global altitude/latitude scale. This variability probably reflects differences in typical size and composition characteristics in the local aerosol content. Depending on altitude and latitude bands, E/B values vary between 25 and 53 sr (see Appendix B.3). Such variability in the E/B values was already reported by Vernier et al. (2011b), although values shown here are lower than the averaged values derived by these authors.

The variability found on E/B led to reconsider the validation of AerGOM (Level 2) and CCI-GOMOS (Level 3) datasets using lidar profiles, by addressing the choice of E/B values. As a next step, the statistical analysis was performed again for co-located CALIOP backscatter values and AerGOM extinction profiles between 2006 and 2009, using E/B values between 30 sr and 70 sr. The outcome of this study and comparison with results by Vernier et al. (2011b) is given in Appendix B.

6. Application to climate modelling

As mentioned previously, a major current issue is to understand the relative impact of volcanoes, of anthropogenic emissions and other aerosol sources on the evolution of the stratospheric aerosol burden. Differences remain between the estimates of the current climate models in terms of radiative forcing, and radiative forcing inferred from satellite measurements (Solomon et al., 2011). Brühl et al. (2015) undertook, in the framework of SPARC/SSIRC (Stratospheric Sulfur and its Role in Climate), a comprehensive inventory of 3-dimensional volcanic SO_2 plumes in the lower stratosphere and uppermost troposphere, to better assess the contribution of volcanoes to the stratospheric aerosol burden. This inventory was based on SO_2 vertical profiles by MIPAS (Höpfner et al., 2015), integrated column SO_2 data from nadir instruments, and reports from the Global Volcanism Program of the Smithsonian Institution (http://volcano.si.edu). For each identified eruption, the inventory provided an estimate of the amount of sulfur gases injected into the stratosphere and uppermost troposphere. This first inventory was then used to estimate the aerosol radiative forcing from 2002 to 2011 by simulating the evolution of the atmosphere using the EMAC chemistry climate model (Jöckel et al., 2006). The result of this simulation showed that significant discrepancies remained with respect to radiative forcing estimated from measurements as reported by Solomon et al. (2011).

This unsatisfactory result tends to confirm that volcanic eruptions of moderate intensity, injecting sulfur gases to the upper troposphere and lower stratosphere, contribute significantly to the stratosphere aerosol layer, as already stated by Vernier et al. (2011b). It also leads to the suspicion that the first version of the volcanic sulfur emission inventory was not sufficient to assess the real volcanic contribution to the radiative forcing of the atmosphere due to lack of data. For this reason, the CCI-GOMOS dataset was used to revise this inventory, by filling gaps in the available datasets, improving estimates of emitted SO_2 for individual volcanic eruptions, and identifying new volcanic signatures in the CCI-GOMOS extinction time series.

xIn this section, we show how the present work contributed to the improvement of the inventory of sulfur emissions by volcanoes and to the modelling of the radiative forcing by stratospheric aerosols. We demonstrate also that GOMOS points to the importance of seasonally varying desert dust in the lowermost stratosphere.

6.1. Methods

6.1.1. The EMAC chemistry climate model

EMAC is an atmospheric chemistry-climate model based on the ECHAM5 general circulation model and the Modular Earth Submodel System (MESSy). It contains a modal aerosol model taking into account 4 soluble and 3 insoluble modes, and allows for the calculation of aerosol optical depth, extinction coefficient, aerosol radiative forcing and feedback to dynamics (Brühl et al., 2015 and references therein). The model considers interactions between aerosol particles and trace gases, and includes also dust and organic material, with a more detailed treatment in the more recent model version. This new version is based on Jöckel et al. (2010) and makes use of the desert dust scheme by Astitha et al. (2012), which causes a strong enhancement of dust transported to the lowermost stratosphere, especially in the Asian Summer Monsoon, as compared to the old version.

6.1.2. The MIPAS dataset

As another atmospheric sounding instrument on ENVISAT, the limb-scanning Michelson Interferometer for Passive Atmospheric Sounding (MIPAS) analyzed the emission of atmospheric species active in the mid-infrared spectral region. Its high spectral resolution (0.025 cm^{-1} and 0.0625 cm^{-1}), allowed the retrieval of volume mixing ratio profiles of sulfur dioxide (SO_2). Two different datasets of SO_2 derived from MIPAS exist: (1) one consisting of monthly 10-degree zonal mean profiles with a vertical coverage of 10–45 km which was derived from mean spectra (Höpfner et al., 2013), and, (2) one dataset retrieved

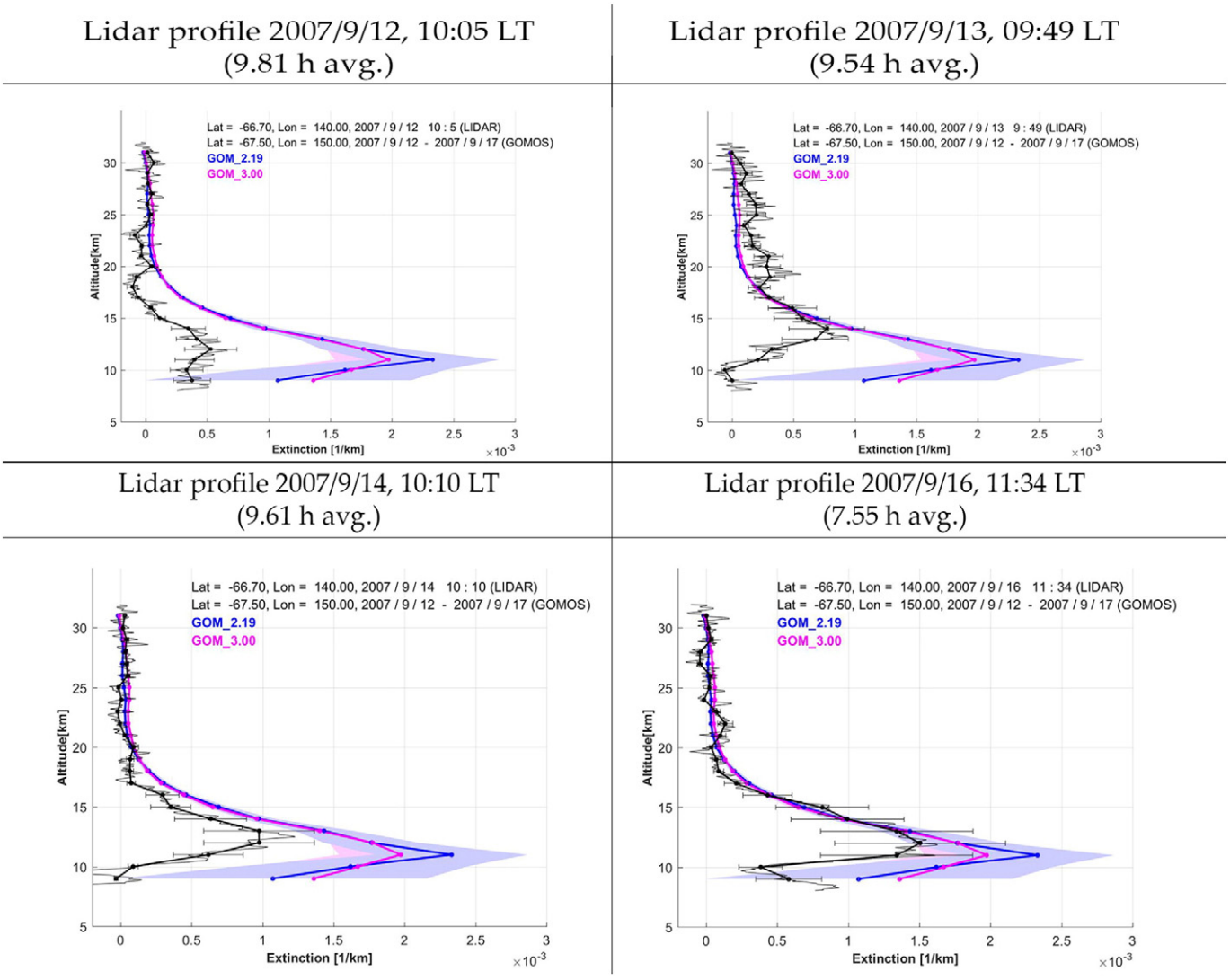

Fig. 8. Intercomparisons of Dumont D'Urville lidar profiles and CCI-GOMOS Level 3 CDRs for the 5-day bin of September 12–17, 2007. The plots show version 3.00 (magenta) and version 2.19 (blue) vertical extinction profiles, and lidar profiles falling in the same time period (black) and showing the development of a PSC around 10–15 km altitude. Magenta and blue regions show the 2-sigma interval across the CCI-GOMOS dataset in versions 3.00 and 2.19, respectively. Lidar error bars indicate the variability of the lidar extinction coefficient for E/B varying between 30 sr and 70 sr and the time in parentheses is the integration time for the lidar measurements.

from single limb-scans with the altitude coverage up to 23 km (Höpfner et al., 2015). The latter data version is suited to analyze the vertical and horizontal evolution of SO_2 plumes from volcanic eruptions, and has been utilized in the study described below. For this application SO_2 was provided with 5-day temporal resolution on a 3D grid similar to the GOMOS data. In December 2016 also data in another retrieval mode were included filling some gaps in 2005 to 2007.

6.2. Improved inventory of volcanic eruptions.

Including the CCI-GOMOS extinction dataset to the other data sources already used in its previous version (Brühl et al., 2015), a new improved inventory was made for the volcanoes contributing to the stratospheric aerosol burden, now three-dimensional. This inventory is presented in Table 7. It contains now about 230 explosive eruptions reaching the tropopause region or higher altitudes for the period July 2002 to March 2012, versus 102 eruptions in the previous inventory (Brühl et al., 2015). Using these two limb viewing instruments covering the same ENVISAT time period was essential to fill data gaps of the individual instruments. In particular, several important eruptions in 2004, 2006 and 2007 could be identified using the CCI-GOMOS dataset, which were not seen by the MIPAS instrument due to lack of data at the corresponding location and time. GOMOS extinctions were converted to SO_2 plumes by application of the parameterization of Grainger et al. (1995) and fit to analogue situations seen by MIPAS, taking into account zonal wind. The attribution to individual eruptions was done based on the Bulletin Reports on http://volcano.si.edu and nadir satellite observations. The SO_2 masses were calculated by integration over the plumes downwind of the volcanoes. Although quantitative estimates of the error are difficult to infer, the most important source of uncertainty resides in the data gaps and in some cases vague observations in the Smithonian bulletins, the typical uncertainty is in the order of about ±30%. Table 7 indicates (last column) which eruptions could be identified and quantified using the MIPAS dataset (M, primary) and which ones, using the GOMOS dataset (G). In case of 'MG' the SO_2-plumes were taken from MIPAS and GOMOS was used to support the attribution process. Examples are given in Appendix C.

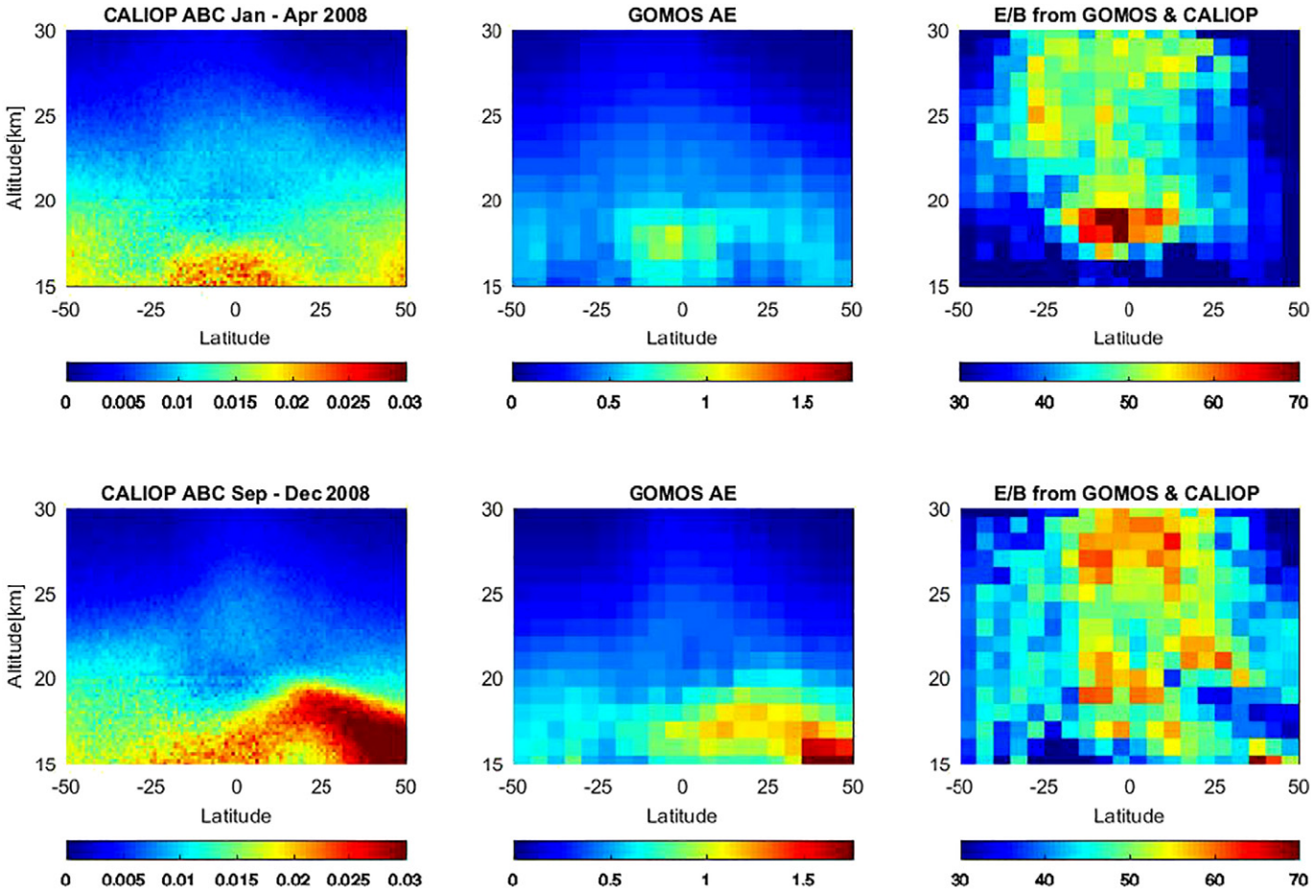

Fig. 9. Comparison between CALIOP (left panel) and CCI-GOMOS version 3.00 (middle panel) zonal mean aerosol extinction coefficients (AE), showing the median for January–April (upper panels) and September–December 2008 (lower panels). The color code shows the aerosol extinction between 0 and 1.75 *10–3 [1/km] (left and middle panel). The right panel shows E/B values recomputed from the CCI-GOMOS extinction coefficient and CALIOP backscatter. In this case, the color bar represents the E/B ratio in sr.

6.3. Comparison of simulations by the EMAC model with GOMOS observations

The data from Table 7 were used, together with other known sources for stratospheric SO_2 to constrain the EMAC model in order to model the evolution of the aerosol burden in the higher troposphere and in the stratosphere, and to evaluate the corresponding radiative forcing. To avoid further uncertainties related to uncertain injection altitude in case of point sources, the observed three-dimensional plumes of SO_2 (volume mixing ratios) are added at the listed times to SO_2 from other sources which include the oxidation of OCS and DMS, and volcanic and anthropogenic SO_2 transported from the troposphere. Fig. 10 shows aerosol extinction coefficients observed by GOMOS (upper pannel) and computed by EMAC from SO_2 and other aerosol sources, including organics and dust from the troposphere, using two model versions. V1 is a version based on Jöckel et al. (2006), while V2 is an updated version using an improved description of desert dust. Note that the meteorology of the model was not constrained by observations so that some deviations due to dynamics are likely. Nevertheless the agreement between this model run constrained using the SO_2 inventory in Table 7 (which only uses fragments of the CCI-GOMOS CDR) and the whole CCI-GOMOS time series (especially with version 3.00, see also Fig. 4) is convincing, showing that EMAC is able to model adequately the global evolution of the aerosol burden based on the volcanic SO_2 inventory. Concerning the contribution of dust, it is visible on Fig. 10 that the simulation with the most recent model version (V2 in Fig. 10) is better than the version based on Jöckel et al. (2006) (V1), which shows an underestimate of extinction in northern hemispheric summer and in the tropopause region. This points to the fact that GOMOS is important for model development.

As a final result from this modelling study, Fig. 11 shows the simulated global radiative forcing of stratospheric aerosol at about 100 hPa. The simulations by Brühl et al. (2015) (black curve) are biased compared to Solomon et al. (2011) (green crosses) who estimated the radiative forcing from satellite extinction measurements (SAGE, CALIOP, GOMOS). Taking more volcanic eruptions into account in the estimate of the total stratospheric aerosol budget, especially during periods where data gaps affect the MIPAS dataset, improves the results considerably (blue curve). Use of a more appropriate scheme for desert dust (V2, red curve and purple crosses) almost removes the bias. The remaining slight bias in years influenced by high latitude eruptions can be removed by inclusion of lower stratospheric aerosol below 100 hPa, but this is also uncertain in Solomon et al. (2011). (For interpretation of the references to color in this figure legend, the reader is referred to the web version of this article.)

7. Conclusions and perspectives

A stratospheric aerosol climate data record has been developed from the GOMOS measurements for the Aerosol_cci project under the Climate Change Initiative. The record consists of gridded aerosol fields (the so-called CCI-GOMOS data records), produced by the binning of Level 2 vertical profiles inverted using the AerGOM algorithm, a retrieval algorithm recently published and which was developed to improve

Table 7
Volcanic SO_2 injections into the stratosphere, derived from MIPAS (M) and OMI/TOMS (Brühl et al., 2015), and updated on the basis of GOMOS (G) extinctions and new MIPAS data (from UTLS mode). In rows marked with "MG", distributions observed by MIPAS are confirmed by GOMOS. Estimates of the total emitted SO_2 mass (6th column) are integrated above 14 km at low latitudes, above 13 km at mid-latitudes and above 12 km at high latitudes. Listed altitudes and latitudes refer to the maxima in MIPAS and GOMOS "volcanic plumes". The given time refers to the center of the first MIPAS 5-day period selected and not to the beginning of the eruption. SO_2 mass estimates are typically inferred from 10-day periods, and for Sarychev and Kasatochi from 30-day periods (with scaling). Some names are abbreviated after their first occurrence in the table. A mention of Vanuatu (or "Van.") without further details means that several volcanoes erupted simultaneously in Vanuatu and could not be separated. A "+" means that the volcanoes cannot be separated or identified. The mention "M" in the first column indicates the presence of monsoon influence.

Volcano or region	Time	Latitude	Longitude	Height (km)	SO_2 3D str (kt)	Obs
Nyamuragira	23 Jul 2002	−1	30	15	23	M
Witori	2 Aug 2002	−6	150	14	18	M
Ruang	26 Sep 2002	2	125	18	71	MG
El Reventador	5 Nov 2002	0	−78	17	77	MG
Nyiragongo, Lokon	9 Jan 2003	−1, 1	30, 125	15, 16	20, 17	MG
Nyirag., Lokon (Rabaul?)	5 Mar 2003	−5, 1	30, 125	17, 15	17, 19	MG
Anatahan, Nyirag., Ulawun	14 May 2003	16, −1, −5	143, 30,150	16, 16, 17	13, 21, 9	M
Lewotobi, Kanlaon	13 Jun 2003	−8, 10	123	15	13, 21	MG
Soufriere Hills	13 Jul 2003	16	−62	15–18	59	MG
Gamalama, Japan, M	17 Aug 2003	1, 33	128, 131	16	15, 13	MG
Bezymianny or Klyuchev.	6 Sep 2003	56	160	14	8	G
Lokon, Soufr.H.(+Masaya)	26 Sep 2003	2, 15	125, −62	16	12, 9	MG
Rabaul	10 Nov 2003	−5	150	16	24	MG
Rabaul	5 Dec 2003	−5	150	16	19	MG
Rabaul, Nyiragongo?	9 Jan 2004	−5, −1	150, 30	17, 15	15, 13	MG
Langila, Nyiragongo?	3 Feb 2004	−5, −1	150, 30	17	16, 4	MG
Soufriere Hills	4 Mar 2004	10	−62	17	28	MG
Nyamu., Awu + Tengger C.	12 Jun 2004	−1, 4, −8	30,125,112	17, 15	25, 22	G
Pacaya, Galeras	17 Jul 2004	15, 1	−91, −77	17	16, 15	G
Galeras	11 Aug 2004	1	−77	16	21	G
Vanuatu, Rinjani + Kerinci	30 Sep 2004	−16, −8, −2	168,116,101	15,15,17	10, 21	G
Manam, Soputan	30 Oct 2004	−4, 1	144, 125	16	11, 16	G
Manam, Nyiragongo	24 Nov 2004	−4, −1	144, 30	17, 15	22, 14	G
Nyiaragongo, Reventador	4 Dec 2004	0	30, −77	16	31, 8	G
Vanuatu, Soputan	24 Dec 2004	−16, 1	168, 125	17, 15	22, 23	G
Manam	28 Jan 2005	−4	144	18	144	MG, M (*)
Anatahan, (+)	3 Apr 2005	16	143	15	21	M
Anatahan, Soufriere Hills	23 Apr 2005	16	143, −62	16	30, 30	M
Anatahan, Fernadina, Van.	18 May 2005	16, 0, −16	143, −91,168	15	11, 15, 8	M
Anatahan, Santa Ana	12 Jun 2005	16, 14	143, −90	15	17, 13	M
Anatahan, Soufriere Hills	12 Jul 2005	16	143, −62	15	18, 13	M
Anatahan, Raung	6 Aug 2005	16, −8	143, 113	15	19, 28	M
Anatahan, Raung	16 Aug 2005	16, −8	143, 113	15	25, 31	MG
Santa Ana	5 Oct 2005	14	−90	17	46	M
Sierra Negra, Dabbahu	25 Oct 2005	−1, −13	−91, 40	15	20, 27	G
Karthala, Galeras	24 Nov 2005	−10, −2	43, −80	16	16, 14	MG
Soputan, Lopevi	24 Dec 2005	1, −16	125, 168	16	33, 18	MG
Rabaul+	23 Jan 2006	−5	152	16	31	MG
Manam, Chile	4 Mar 2006	−5, −40	144, −70	17	72, 7	MG
Cleveland	14 Mar 2006	53	−170	13	8	G
Ecuad., Tinakula, Lascar	18 Apr 2006	−5,-10, −23	−78,166, −68	17	16, 21, 3	M
Soufriere Hills	23 May 2006	16	−62	19	156	MG
Kanlaon	2 Jul 2006	10	123	20	70	M
Tungurahua, Rabaul	16 Aug 2006	−2, −4	−78, 150	19	44, 22	MG
Rabaul	10 Oct 2006	−4	150	17	172	M
Ubinas, Vanuatu	25 Oct 2006	−20	−70, 168	17, 15	14, 41	M
Ambrym	9 Nov 2006	−10	160	17, 15	45	M
Nyamuragira, Mexico	29 Nov 2006	5	30, −90	17, 15	40, 30	MG
Bulusan, Soputan, Vanuatu	24 Dec 2006	13, 1, −16	125,125,168	18, 16, 15	10, 10, 18	MG
Karthala, Bulusan, Lascar, Shiveluch, Vanuatu	23 Jan 2007	−10, 13, −23, 57, −16	43, 125,-68, 160, 168	17,17,15, 15,15	6, 5, 7, 8, 6	MG
Nev. d Huila, Kartha., Van.	22 Feb 2007	0, −10, −16	−70, 43, 168	16,15,16	11, 14, 11	MG
Etna, Reventador, Ambrym	24 Mar 2007	38, 0, −16	15, −78, 160	15,16,17	11, 24, 20	MG
Pit.Fourn.Reunion, Reventador +	8 Apr 2007	−20, 0	57, −80	16	31, 15	MG
Ulawun,Vanuatu,N.d.Huila	3 May 2007	−5, −25, 3	150,160, −70	15	15, 7, 9	MG
Papua, Kamchatka, Nyira., Ubinas + Lascar	13 May 2007	−10, 50, 0, −20	150,150,30, −75	16	8, 1, 13, 8	MG
Llaima,Vanuatu, Bulusan	23 May 2007	−30, −15, 13	−70,160,125	18,15,17	14, 8, 10	MG
Soputan,Bezym.,Telica	12 Jun 2007	1, 56, 13	125,160, −87	16, 14,15	19, 10, 13	MG
Lengai, Mexico, M	2 Jul 2007	2, 20	29, −90	16, 15	17, 11	M
Raung, Japan, M (+)	27 Jul 2007	−5, 35	110, 130	15	14, 14	M
Manda Hararo, Java, M	11 Aug 2007	12, −5	40, 115	17, 15	21, 18	M
Vanuatu, Mexico, M	20 Sep 2007	−5, 20	180, −90	16	11, 18	M
Jebel al Tair, Galeras	5 Oct 2007	15–40(16), 1	42, −80	16	68, 13	M
Galeras, Jebel, Soputan	4 Nov 2007	−2, 15, −5	−80,42,110	16	10, 7, 12	MG
Soputan or Krakatau, Galeras, Chikurachki	14 Nov 2007	−5, −1, 50	110, −75,155	16,16, 15	13, 12, 45	M
Talang, Galeras	9 Dec 2007	0	100, −75	16	13, 15	M
Ulawun?	19 Dec 2007	1	150	17	29	MG

(continued on next page)

Table 7 (*continued*)

Volcano or region	Time	Latitude	Longitude	Height (km)	SO_2 3D str (kt)	Obs
Nevado del Huila, Llaima	3 Jan 2008	1, −35	−71	17, 15	32, 5	M
Galeras, Anatahan	23 Jan 2008	−3, 15	−80, 145	16	24, 12	M
Tungurahua, Papua	12 Feb 2008	−5	−80, 155	16, 17	19, 14	M
TaraBatu (+)	13 Mar 2008	−5	125	16	33	MG
Lengai, Andes, Kerinci	28 Mar 2008	−5, 5, −2	36, −80, 101	16	10, 7, 11	M
Egon, Nev.d.Huila	12 Apr 2008	−5, 5	122, −76	15, 17	20, 13	M
Mexico, Ibu, Chaiten	27 Apr 2008	15, −35	−90, 125, −70	16	13, 15, 4	M
Mexico, Barren I., Chaiten	12 May 2008	10, −35	−90, 90, −70	16, 14	13, 18, 6	M
Soputan, Nicaragua/C.R.	16 Jun 2008	1, 15	125, −85	16	32, 10	M
Okmok, Soputan	21 Jul 2008	53, 1	−168, 125	16	57, 30	M
Kasatochi	15 Aug 2008	52	−175	13–18	390	MG
Dallafilla,N.d.Huila,Rev.	13 Nov 2008	14, 3	40, −78	17	55, 40	M
Karangetang, Galeras, Japan	18 Dec 2008	3, 0, 30	125, −80,130	17, 17, 15	19, 13, 11	MG
Barren Island, Galeras	2 Jan 2009	10, 3	90, −80	17, 15	16, 16	M
Indonesia?, Galeras	27 Jan 2009	−5, 0	100, −80	16	15, 13	M
Galeras, Villarrica, Karangetang, Vanuatu	16 Feb 2009	−2, −35, 3, −16	−78, −75, 100, 168	16, 15, 16, 17	12, 7, 7, 8	M
Redoubt, Galeras	28 Mar 2009	60, 0	−155, −75	13, 15	61, 43	M
Fernandina, Nyira.	12 Apr 2009	0	−90, 30	16	12, 16	M
Galeras + Reventador	7 May 2009	0	−75	15	31	M
Rinjani, Vanuatu, Revent.	22 May 2009	−5, −15, 3	116,165, −80	16	5, 6, 18	M
Sarychev, MandaHararo	21 Jun 2009	48, 12	153, 40	16	496, 91	MG
Vanuatu, Mayon, Galeras	4 Oct 2009	−15, 13, 2	165,120, −80	17	6, 9, 14	M
Tungurahua, Hawaii, Van.	19 Oct 2009	5, 20, −16	−76, −155, 165	16	11, 8, 9	MG
Galeras, Karkar, Vanuatu	3 Dec 2009	0,-5,-16	−78,146,165	17	15, 12, 5	M
Mayon, Nyamuragira, Van.	2 Jan 2010	13, 0, −15	120, 30, 168	16	12, 12, 13	M
Turrialba, Vanuatu	17 Jan 2010	5, −15	−82, 168	16	15, 15	M
Soufriere Hills +	16 Feb 2010	16	−62	16–18	46	M
Arenal, Indon., Van.	2 Apr 2010	9, 0, −16	−84,120,168	15	18, 15, 6	M
Tungurahua, Dukono, Van.	2 May 2010	−5, 2,-16	−78,128,168	16	20, 14, 10	M
Pacaya, Ulawun, Sarigan	6 Jun 2010	15, −5, 16	−91,150,145	17, 16, 15	38, 8, 6	M
Ulawun, Costa Rica, Miyakejima, M	16 Jul 2010	−5, 15, 35	150, −87, 140	16	11, 18, 8	MG
Karanget., Nicaragua, Van.	15 Aug 2010	3, 15, −16	125, −85,168	16	17, 17, 9	M
Galeras, Sinabung M	30 Aug 2010	5	−77, 100	16	16, 20	M
Karangetang?, Barren Isla.	4 Oct 2010	3, 12	125, 94	16	28, 19	M
Merapi	8 Nov 2010	−7	110	17	108	M
Tengger C., Tungu., Chile	23 Dec 2010	−8, −3, −40	110, −78, −75	17	23, 19, 12	M
Tengger C.	7 Jan 2011	−8	110	16	40	M
Lokon-Empung, Planchon, Bulusan	26 Feb 2011	1, −35, 13	125, −75,125	16, 15, 16	19, 5, 17	M
Karangetang, Sangay, Planchon	23 Mar 2011	2, −2, −35	125, −78, −75	15	12, 12, 6	M
Galeras?, Karangetang	12 Apr 2011	5	−77, 128	16	14, 13	M
Tungurahua, Dukono, Van.	2 May 2011	2, 2, −16	−78,128,160	16, 16, 15	18, 13, 7	M
Grimsvötn, Lokon	27 May 2011	65, 1	−20, 125	14, 16	20, 30	M
Puyehue	11 Jun 2011	−41	−71	13	23	G
Nabro	21 Jun 2011	10–55 (13)	41	16–19	446	MG
Soputan, Marapi	20 Aug 2011	1, 0	125, 100	18, 16	15, 5	MG
Manam, Tungurahua	19 Oct 2011	−4, −3	144, −78	16	14, 14	M
Nyamuragira	18 Nov 2011	−2	29	16	39	M
Gamalama, Nyamuragira	18 Dec 2011	1, −1	128, 29	16, 15	27, 19	M
Vanuatu, Nyamuragira	12 Jan 2012	−16, −1	168, 29	16, 14	20, 17	M
Vanuatu, Nyamuragira	11 Feb 2012	−16, −1	168, 29	17	23, 22	M
N.·Ruiz, Marapi	12 Mar 2012	−3, 0	−76, 100	16, 17	17, 21	M

(*) MG: if using CCI-GOMOS, v. 2.19; M: if using CCI-GOMOS, v. 3.00.

and optimize the aerosol retrieval from GOMOS. Taking into account the variable quality of the GOMOS measurements depending on the star and orbital parameters (star magnitude and temperature, solar zenith angle, etc.), selection criteria are applied to ensure high quality of the gridded aerosol properties products.

Among the various parameters included in this record and presented in Table 3, this paper focuses on the aerosol extinction time series, provided at five wavelengths.

Investigation of the influence of the star properties on the uncertainty in the extinction coefficient retrieval by considering limiting cases of bright/dim, hot/cool stars, showed that the influence of the star magnitude dominates the uncertainty on the extinction coefficient, the brightest stars (magnitude < 1.5) providing uncertainties generally smaller than ~30% while the dimmest stars (magnitude > 2.6) leading to uncertainties in the range 30–60%. The star temperature also influences the uncertainty in the extinction coefficient retrieval, but to a lesser extent, with the lowest (highest) uncertainties found for hot (cool) stars.

During the course of the project, several improvements were implemented into the AerGOM algorithm, which are discussed in the paper. The implementation of the spectral retrieval was revised to provide a better convergence of the optimization process to a realistic solution, also in cases where the star's signal is very faint and the information content low (i.e. typically for dim cool stars). Further, a revision of the molecular absorption cross-section spectra used for the spectral retrieval of the gas species led to a more realistic attribution of the extinction coefficient to aerosol and gas species, resulting in a significantly fewer negative values of the aerosol extinction coefficient, especially at high altitudes.

The AerGOM (Level 2) dataset and the CCI-GOMOS (Level 3) dataset were evaluated successively using lidar profiles from 3 ground-based lidar station representative for different typical regions: Mauna Loa situated in the tropical region, Garmisch-Partenkirchen representative for northern mid-latitudes, and the Antarctic station of Dumont d'Urville. For this latter station, separate statistical analyses of Level 2 profiles were performed for background aerosols and for PSCs as identified by

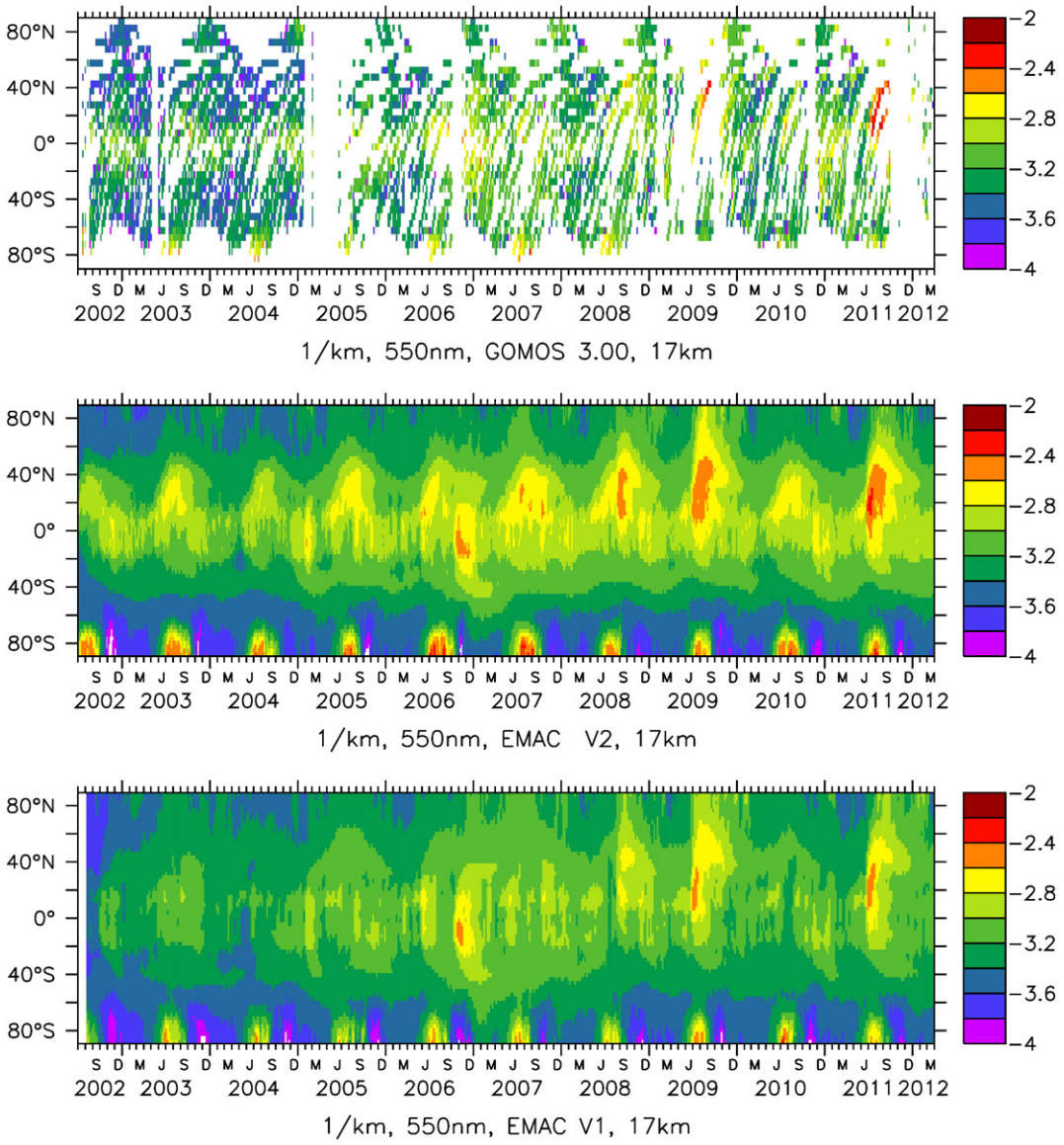

Fig. 10. Aerosol extinction coefficient as observed by GOMOS (upper panel) and simulated by EMAC (550 nm, 17 km, decadal logarithm) in two versions (V1, lower panel and V2, central panel).

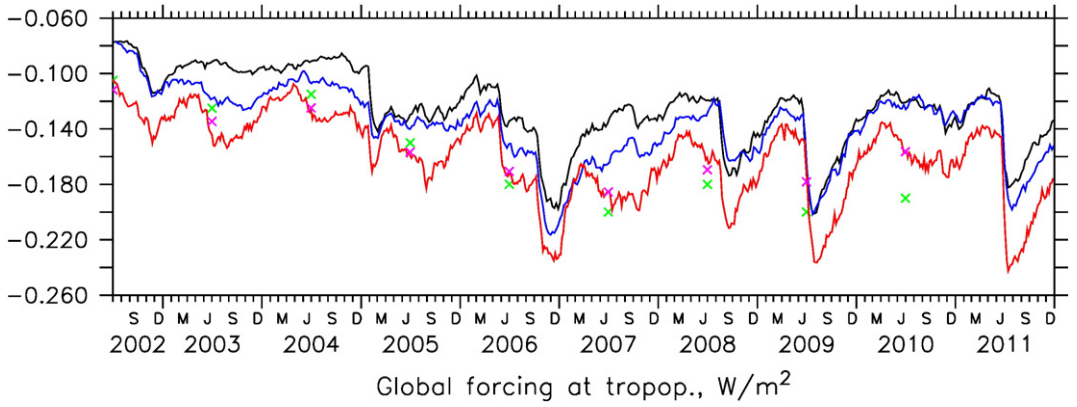

Fig. 11. Stratospheric aerosol radiative forcing simulations; in blue: simulation using all eruptions reported in Table 7; in black: simulation with less eruptions as given in Brühl et al. (2015). Green crosses show annual average radiative forcing estimates derived from observations by Solomon et al., 2011. The red curve (simulated radiative forcing) and the purple symbols (corresponding annual average) show the results obtained using the V2-simulation (with entries of Table 7 and an improved desert dust scheme).

the GOMOS aerosol type flag using a selection criterion based on the temperature. Intercomparisons using lidar profiles from the Garmisch-Partenkichen dataset show a better agreement in the case of the Level 3 evaluation than for the Level 2 assessment. Good agreement between AerGOM and lidar data was found in the case of Mauna Loa and Dumont d'Urville (uncertainty in the range 1%–35%) below 22 km. This evaluation shows, overall, similar results for the CCI-GOMOS time series in version 2.19 (with more restrictive criteria for the observation selection) and version 3.00 (with relaxed selection criteria). This validates the selection criteria of the last version (3.00), which provide a much better data coverage than version 2.19.

A careful analysis of the results of all these intercomparisons pointed to several factors, which can alter the result of the validation. These factors are mainly: (1) the possible difference in air masses sounded by the compared profiles due to a spatio-temporal mismatch or to a difference in viewing angle; (2) the rapidly varying features of certain aerosol patterns, more particularly in the case of PSCs; (3) an inadequate value of the lidar ratio in the lidar extinction derivation. To test this latter possibility, the CCI-GOMOS Level 3 was compared with CALIOP data available on a global scale. Calculating the ratio between the GOMOS extinction coefficient and the CALIOP backscatter showed that the lidar ratio varies as a function of altitude and latitude, emphasizing the need to adapt the E/B value to the latitude and altitude range. This result confirms observations made previously by Vernier et al. (2011b), although the E/B estimates found in the present work are generally lower than the ones found by these authors. This detailed statistical assessment and the investigation of the results of intercomparison lay more robust grounds to continue the validation of the CCI-GOMOS CDRs in the near future.

The characteristics and performance of the CCI-GOMOS climate data records evolved during the course of the Aerosol_cci project according to these investigations and improvements, and as a result of the feedbacks from the User team. The use of monthly means was abandoned for 5-days time intervals, better suited for the identification of aerosols plumes and the quantification of the emitted sulfur species emitted by volcanic eruptions. Latitude and longitude grid resolutions were revised to describe the effect of atmospheric motion in a more coherent way within this time interval. Algorithm improvements allowed relaxing the observation selection criteria ensuring a sufficient data quality, while searching for the best trade-off between sufficient data quality and maximum data coverage.

The use of the CCI-GOMOS climate data record in combination with MIPAS SO_2 time series led to an update of the volcanic sulfur emission inventory used to model the evolution of the stratospheric aerosol concentration during the post-2000 period. About 230 explosive eruptions could be identified, and their impact on the aerosol load, quantified. An overview of these eruptions, including the plume height and an estimate of the emitted SO_2 content, is presented in Table 7.

The updated inventory of volcanic emissions was then used in the EMAC model in order to simulate the evolution of the stratospheric aerosol concentration and to calculate the corresponding radiative forcing. Comparisons of the modelled aerosol burden with the CCI-GOMOS extinction field over the whole time period show a good agreement between both datasets, and the estimate of the radiative forcing from EMAC using the updated inventory better matches radiative forcing estimated from observations published by Solomon et al. (2011), than previous estimates published by Brühl et al. (2015). This holds especially for the simulation with improved desert dust (V2). This successful application confirms that the CCI-GOMOS climate data records developed using the AerGOM retrieval algorithm can be used successfully in climate modelling applications.

Abbreviations

The following abbreviations are used in this manuscript:

AAI	absorbing aerosol index
ACE	atmospheric chemistry experiment
ADM	atmospheric dynamics mission
AerGOM	GOMOS retrieval algorithm optimized for aerosols
AOD	aerosol optical depth
ATSR	along track scanning radiometer
BSR	backscatter ratio
CALIOP	cloud-aerosol lidar with orthogonal polarization
CALIPSO	cloud-aerosol lidar and infrared pathfinder satellite observations
CCI	climate change initiative
CDR	climate data record
DMS	dimethyl sulfide
DOAS	differential optical absorption spectroscopy
ECV	essential climate variable
EMAC	ECHAM/MESSy atmospheric chemistry model
ENVISAT	ESA's environmental satellite
ESA	European space agency
E/B	extinction to backscatter ratio
GCOS	global climate observing system
GMAO	global monitoring and assimilation office
GOME	global ozone monitoring experiment
GOMOS	global ozone monitoring by occultation of stars
IASI	infrared atmospheric sounding interferometer
IPF	instrument processor facility; operational GOMOS retrieval algorithm
IQM	interquartile mean
IQR	interquartile range
L2	level 2, satellite sensor projected data
L3	level 3, gridded satellite dataset
IPCC	intergovernmental panel on climate change
K	Kelvin
MAESTRO	measurements of aerosol extinction in the stratosphere and troposphere retrieved by occultation
MESSy	modular earth submodel system
MIPAS	Michelson interferometer for passive atmospheric sounding
NDACC	network for the detection of atmospheric composition change
NO_2	nitrogen dioxide
NO_3	nitrate
OCS	carbonyl sulfide
OMI	ozone monitoring instrument
OSIRIS	optical, spectroscopic, and infrared remote imaging system
O_3	ozone
POAM	polar ozone and aerosol measurement
PSC	polar stratospheric cloud
PSD	particle size distribution
SAA	southern atlantic anomaly
SAGE	stratospheric aerosol and gas experiment
SCIAMACHY	scanning imaging absorption spectrometer for atmospheric chartography
SNR	signal-to-noise ratio
SO_2	sulfur dioxide
SPA	GOMOS spectrometer A
SPB	GOMOS spectrometer B
SPARC	stratospheric processes and their role in climate
SSiRC	stratospheric sulfur and its role in climate
SZA	solar zenith angle
TOMS	total ozone mapping spectrometer
UV	ultraviolet
V1, V2	different versions of the EMAC model (See §6.2 for more details)

Acknowledgments

This work was supported by the European Space Agency as part of the Aerosol_cci project (ESA Contract No. 4000109874/14/I-NB).

Supporting work for the development of GOMOS datasets was performed in the framework of a Marie Curie Career Integration Grant within the 7th European Community Framework Programme under grant agreement no. 293560. We thank the ICARE Data and Services Center for providing development support and tools. We thank Dr. Ann-Carine Vandaele for her support and fruitful discussions concerning the revision of the cross-section database. Parts of the modelling work were supported by the EU project STRATOCLIM. Lidar observations at Dumont d'Urville are supported by the French Polar Institute IPEV.

Appendix A. Elaboration of a new cross-section database for AerGOM

As discussed in Section 2.4, the gas absorption cross-sections spectra used for the retrieval of the gas species have been completely revised in order to improve their spectral range, temperature dependence, and to optimize the consistency of the data for the whole range of wavelengths and temperatures encountered in GOMOS measurements. The aim of this appendix is to provide details on the methodology used to elaborate the new cross-section spectra from the available datasets and for the different gas species retrieved so far by AerGOM: O_3, NO_2 and NO_3. We limit here the discussion to the spectral range of interest for this paper, i.e. the spectral range covered by the GOMOS spectrometers SPA and SPB1 (See Section 2).

A.1. Ozone

Serdyuchenko et al. (2014) published high-resolution ozone absorption cross-sections covering the 213–1100 nm spectral range over the temperature range 193–293 K which covers the whole range of experimental conditions encountered by GOMOS with a spectral resolution higher than the GOMOS resolution (See Section 2.1), ensuring an optimal consistency for use in the spectral inversion.

A.2. NO_2

The case of NO_2 requires the use of different sets of measurements. Vandaele et al. (2003) propose a unified dataset set up from various previous measurements, resulting in two (medium resolution and a high resolution) recommended spectra. The medium resolution absorption spectrum spans the 13,200–42,000 cm^{-1} spectral range (238–757.8 nm) with a spectral resolution of 2 cm^{-1} (0.01–0.11 nm), higher than the spectral resolution of the GOMOS SPA spectrometer. At this resolution, no pressure effect is detectable. The temperature is described using a linear dependence. By its composite character, this dataset is expected to be less sensitive to experimental noise due to the use of an average of many different profiles. All these features make it adequate for use in AerGOM in the range 240–695 nm. The high-resolution proposed by Vandaele et al. (2003) is mainly based on (Vandaele et al., 2002) and provided at three different temperatures (220, 240 and 294 K) with a spectral resolution of 0.05 cm^{-1} (0.002–0.003 nm) over the range 689.6–757.8 nm, which is higher than the GOMOS SPB1 spectral resolution and hence well adapted for use in the AerGOM retrieval. At each wavelength, the cross-sections at the three temperature values are used to compute a linear temperature dependence using a least square fit. Pressure effects are observed on the cross-section for these spectral range and resolution, and the authors provide an expression describing the broadening of the spectral range in high-pressure conditions. The potential impact of this broadening on GOMOS measurement was investigated, and it appeared that the pressure effect is totally smoothed out when the NO_2 absorption spectrum is degraded at the resolution of the GOMOS SPB1 spectrometer. Hence, the high-resolution NO_2 cross-section spectrum proposed by Vandaele et al. (2003) can be used in the 750–757.8 nm range without taking pressure effects into account. Again, this dataset is preferred to Vandaele et al. (2002) because of the use of averaging making it less sensitive to experimental noise. Above 757.8 nm, the only dataset available is the one from Vandaele et al. (1998) measured with a spectral resolution of 2 cm^{-1} (0.11–0.12 nm) and provided at temperatures of 220 and 294 K. Although this resolution is slightly lower than the SPB1 spectral resolution, it is the best choice available for this spectral range. The temperature dependence is calculated by linear interpolation of the two provided spectra.

A.3. NO_3

Orphal et al. (2003) measured NO_3 high-resolution absorption spectra in the range 12,600–21,500 cm^{-1} (476–794 nm) at 294 K with a resolution of 0.6 cm^{-1} (0.01–0.04 nm). The authors investigated in detail the temperature dependence around the absorption peak at 662 nm and proposed a model of temperature dependence valid around this peak (650–675 nm). This work improves the previous measurements in terms of calibration and spectral resolution, including measurements by Yokelson et al. (1994) at four temperatures over the range 400–694 nm and with a resolution of about 0.1 nm. Also, measurements by Sander (1986) at 230 and 298 K covering the 400–691 nm range have a lower resolution (1 nm). Other NO_3 reference cross-section spectra were considered but appeared to be combinations and/or normalized spectra based on (Sander, 1986). Below 400 nm, only very sparse measurements from (Sander, 1986) are available.

In the revision of the cross-section database, the NO_3 high-resolution cross-section spectrum from (Orphal et al., 2003) is used in the whole available range. Orphal's temperature dependence model is also used between 650 nm and 675 nm. Between 476 and 694 nm, a choice must be made between Yokelson's dataset for which the temperature dependence is available and Orphal's dataset with improves the data quality, but is only given at 294 K. The decision was made to use, at each wavelength, a temperature dependence calculated from (Yokelson et al., 1994) and to apply it to NO_3 cross-section profiles from (Orphal et al., 2003). Wherever no data are provided by Yokelson et al. (1994) in the spectral range 476–794 nm (i.e. in temperature range 200–220 K and the spectral range 694–794 nm), Orphal's values at 294 K are used at all temperatures. Between 440 and 476 nm, we dispose on data from (Yokelson et al., 1994) at four temperatures, and lower-resolution data at two temperatures from (Sander, 1986). Comparisons between all available datasets showed that the cross-section spectra provided from (Yokelson et al., 1994) diverge from the other available reference spectra (Sanders' data and other recommended spectra based on Sanders). Therefore, it was decided to use Sander's NO_3 cross-section spectra at 298 K and to apply again Yokelson's temperature dependence wherever it is available. Below 220 K, the temperature dependence is unknown and the cross-section values at 220 K are used down to 200 K. The effective spectral resolution in the range 440–476 nm is thus Sanders' low resolution of 1 nm, which is lower than the SPA resolution, but it was the best solution to avoid any significant jump in the cross-section spectrum. Below 400 nm, the very sparse measurements from (Sander, 1986) are not considered and the NO_3 cross-section spectrum is kept constant and equal to its value at 400 nm. In order to definitely prevent any abrupt jumps between datasets, wavelengths over an

interval equal to two times the resolution of the spectrometer (0.8 nm for spectrometer SPA and 0.13 nm for spectrometer SPB, see Section 2.1) around the transition points were not taken into account.

Appendix B. Dependence of the validation results in the choice of aerosol extinction to backscatter ratio

As discussed in Section 5, the aerosol extinction to backscatter ratio E/B used for the conversion of lidar backscatter in an extinction profile depends on the aerosol type. Since E/B is not well known but determines in a critical way the result of the comparison between the lidar and the validated profiles, the evaluation of the AerGOM Level 2 and CCI-GOMOS Level 3 datasets was repeated for different choices of E/B: 30 sr, 50 sr, and 70 sr. The second value (50 sr) is a standard value used for such conversion, and the two other choices are values, which may be representative for more extreme cases of aerosol conditions. This appendix presents the statistical analysis of the validation performed with these 3 values of the aerosol extinction to backscatter ratio. In addition, E/B estimates from the GOMOS/CALIOP ratio are shown for the three four-months periods in 2008.

B.1. Statistics for level 2 comparisons

Tables B1 to B5 present, for E/B values of 30 sr, 50 sr, and 70 sr, the median, interquartile mean (IQM), which is the average of all values between percentiles 25 and 75, and interquartile range (IQR), which is the difference between the 25th and 75th percentile, of the relative difference in % between AerGOM and the lidar data, (AerGOM-LIDAR)/LIDAR. These statistical analyses refer to the lidar time series measured at Garmisch-Partenkirchen (Table B1), Mauna Loa (Table B2), and Dumont d'Urville (Table B3 to Table B5) respectively. The three statistical indicators are averaged over altitude ranges 10–15 km, 16–21 km, and 22–27 km, taking into account only AerGOM events with a sufficient quality. The selection criteria are the ones used to process versions 2.19 and 3.00 of the CCI-GOMOS CDR, as given in Table 5. This estimation of E/B is repeated for these two sets of selection criteria, and for the criteria used in the "BEST" case (test selection assuming very conservative observation selection criteria) defined in Section 5.2. The observation selection criteria for the "BEST" case are: Star magnitude < 2 SZA > 105° and Star temperature > 5000 K. In all cases, we use here the AerGOM dataset, version 3.0.

Table B1
Comparisons between AerGOM and lidar at Garmisch-Partenkirchen. Shown are the median (M), interquartile mean (IQM) and interquartile range (IQR) of the relative difference between AerGOM and the lidar data, in %. The columns refer to different event selection criteria, and the rows, to different altitude ranges (see explanations in the text).

GARMISCH-PARTENKIRCHEN — Level 2										
E/B ratio		50 sr			30 sr			70 sr		
Altitude/criteria		BEST	2.19	3.00	BEST	2.19	3.00	BEST	2.19	3.00
22–27 km	M	118	96	107	257	213	226	53	34	40
	IQM	112	131	149	240	245	265	46	48	57
	IQR	67	131	149	111	205	223	48	88	96
16–21 km	M	71	75	81	185	191	202	22	25	30
	IQM	51	74	81	152	190	202	8	24	29
	IQR	48	151	134	80	252	224	34	108	96
10–15 km	M	−51	19	83	−22	94	191	−67	−17	25
	IQM	−51	−27	118	−22	17	259	−67	−50	54
	IQR	381	345	341	611	555	537	262	238	230

Table B2
Same as Table B1, for comparisons between AerGOM and lidar at Mauna Loa (shown are the median, IQM and IQR).

MAUNA LOA — Level 2										
E/B ratio		50 sr			30 sr			70 sr		
Altitude/criteria		BEST	2.19	3.00	BEST	2.19	3.00	BEST	2.19	3.00
22–27 km	M	−11	−13	−9	48	44	52	−36	−38	−35
	IQM	−12	−14	−2	47	44	63	−37	−38	−30
	IQR	30	34	53	49	57	88	21	24	38
16–21 km	M	−24	−34	−32	27	11	14	−45	−53	−51
	IQM	−23	−28	−18	28	19	37	−45	−49	−41
	IQR	53	56	64	89	93	107	38	40	46
10–15 km	M	–	–	–	–	–	–	–	–	–
	IQM									
	IQR									

Table B3
Same as Table B1, for comparisons between AerGOM and lidar at Dumont D'Urville (shown are the median, IQM and IQR), here for all aerosol types.

DUMONT D'URVILLE — Level 2										
All aerosol types										
E/B ratio		50 sr			30 sr			70 sr		
Altitude/criteria		BEST	2.19	3.00	BEST	2.19	3.00	BEST	2.19	3.00
22–27 km	M	−32	−35	−34	14	9	10	−51	−53	−53
	IQM	64	71	5	173	186	74	17	22	−25
	IQR	181	157	172	301	261	286	129	112	123
16–21 km	M	−19	−24	−20	35	27	33	−42	−46	−43

Table B3 (*continued*)

DUMONT D'URVILLE — Level 2										
All aerosol types										
E/B ratio		50 sr			30 sr			70 sr		
Altitude/criteria		BEST	2.19	3.00	BEST	2.19	3.00	BEST	2.19	3.00
	IQM	10	−15	74	83	42	190	−22	−39	24
	IQR	76	76	99	127	126	166	54	54	71
10–15 km	M	5	3	10	74	71	83	−25	−27	−22
	IQM	33	25	93	122	108	221	−5	−11	38
	IQR	86	84	165	143	140	275	61	60	118

Table B4
Same as Table B1, for comparisons between AerGOM and lidar at Dumont D'Urville (shown are the median, IQM and IQR), here for profiles with PSCs.

PSCs										
E/B ratio		50 sr			30 sr			70 sr		
Altitude/criteria		BEST	2.19	3.00	BEST	2.19	3.00	BEST	2.19	3.00
22–27 km	M	−28	−30	−36	20	16	7	−49	−50	−54
	IQM	87	64	207	212	173	412	34	17	120
	IQR	181	154	151	302	257	252	130	110	108
16–21 km	M	−30	−30	−28	17	16	20	−50	−50	−49
	IQM	−11	−14	5	48	43	74	−37	−39	−25
	IQR	60	61	77	100	101	128	43	43	55
10–15 km	M	2	−2	0	63	63	67	−30	−30	−28
	IQM	11	11	42	85	85	137	−21	−21	1
	IQR	52	50	112	86	83	186	37	36	80

Table B5
Same as Table B1, for comparisons between AerGOM and lidar at Dumont D'Urville (shown are the median, IQM and IQR), here for background aerosol profiles, supposed to consist only of sulfate aerosols.

Background aerosols										
E/B ratio		50 sr			30 sr			70 sr		
Altitude/criteria		BEST	2.19	3.00	BEST	2.19	3.00	BEST	2.19	3.00
22–27 km	M	−39	−39	−33	1	1	11	−57	−57	−52
	IQM	−38	70	−484	4	183	−740	−55	21	−374
	IQR	130	189	237	217	314	396	93	135	170
16–21 km	M	10	1	16	84	69	93	−21	−28	−17
	IQM	57	−30	229	161	17	448	12	−50	135
	IQR	120	118	199	201	197	331	86	85	142
10–15 km	M	27	13	66	112	89	177	−9	−19	19
	IQM	27	50	240	175	150	467	18	7	143
	IQR	65	155	246	256	258	409	110	111	175

The discrepancies between AerGOM and lidar datasets can be due to two different reasons: (1) a bias of AerGOM profiles with respect to the reference lidar profiles, and (2) an inappropriate choice of E/B.

In the case of Garmisch-Partenkirchen (Table B1), AerGOM is potentially overestimated with respect to the lidar dataset. From Table B1, the best choice of E/B is 70 sr at all altitudes. The results are very consistent between 2.19 and 3.00; at lower altitudes, the consistency is good between versions BEST and 2.19, but less satisfactory with version 3.00.

The evaluation using Mauna Loa time series (Table B2), shows the best agreement between lidar and AerGOM co-located events for E/B = 50 sr at all altitude ranges. AerGOM and the lidar dataset show a good agreement, and there is a good consistency between the statistics calculated for the 3 versions (2.19, 3.00 and BEST), which seems to confirm the appropriateness of the observation selection criteria in both versions 2.19 and 3.00.

In the case of the Antarctic Dumont d'Urville station (Tables B3 to B5), separate statistical analyses are performed for the PSC occurrences and for background sulfate aerosols. In both cases, the AerGOM aerosol type flag provides the aerosol type, and the corresponding extinction values are compared with all available co-located lidar profiles at the same altitude.

In the case of PSCs, choices E/B = 50 sr and E/B = 70 sr give the best agreement. Further, a finer discrimination of the PSC type would be needed from the AerGOM aerosol type flag for an optimal choice of E/B and more detailed comparison. Results are very consistent for the 3 versions 2.19, 3.00 and BEST, indicating again a satisfactory choice of the observation selection criteria for both CCI-GOMOS versions 2.19 and 3.00.

For case of background aerosols, the choice E/B = 30 sr seems to provide a less favourable statistical analysis: both other cases (E/B = 50 sr and E/B = 70 sr) give overall a better agreement between lidar and AerGOM. There is overall a good agreement between the statistical results for all 3 versions.

B.2. Statistics for level 3 comparisons

Tables B6 to B8 show, for E/B = 30 sr, 50 sr, and 70 sr, similar quantities as previously (statistics on Level 2, Section B1) for the CCI-GOMOS level 3 dataset. Again, the statistical analyses refer to the lidar stations at Garmisch-Partenkirchen (Table B6), Mauna Loa (Table B7), and Dumont d'Urville (Table B8) respectively. The comparisons are made for CCI-GOMOS level 3 datasets in versions 2.19 and 3.00, and are given as the median, interquartile mean (IQM) and interquartile range (IQR) of the relative difference between CCI-GOMOS and the lidar data (GOMOS-LIDAR)/LIDAR [%]. As before, averaging is performed over 3 altitude bands corresponding to the ranges 10–15 km, 16–21 km, and 22–27 km.

Table B6
Comparisons between CCI-GOMOS and lidar at Garmisch-Partenkirchen (shown are the median, IQM and IQR). Values of the E/B ratio provided by NDACC are typically about 40–50 sr in the stratosphere, and 10–70 sr in the 5–14 km altitude range.

GARMISCH-PARTENKIRCHEN — Level 3							
E/B ratio		From NDACC		30 sr		70 sr	
Altitude/version		2.19	3.00	2.19	3.00	2.19	3.00
22–27 km	M	61	94	144	192	5	25
	IQM	117	164	193	243	25	47
	IQR	157	161	252	263	108	113
16–21 km	M	16	46	94	144	−17	4
	IQM	39	69	131	181	−1	21
	IQR	104	122	174	202	754	87
10–15 km	M	−49	7	−17	69	−64	−27
	IQM	−147	61	102	288	−73	66
	IQR	163	244	177	360	76	154

Table B7
Comparisons between CCI-GOMOS and lidar at Mauna Loa (shown are the median, IQM and IQR).

MAUNA LOA — Level 3							
E/B ratio		50 sr		30 sr		70 sr	
Altitude/version		2.19	3.00	2.19	3.00	2.19	3.00
22–27 km	M	−18	−12	36	47	−42	−37
	IQM	−13	−2	46	63	−38	−30
	IQR	36	41	59	68	25	29
16–21 km	M	−41	−39	−2	1	−58	−57
	IQM	−38	−22	3	30	−56	−44
	IQR	42	49	70	82	30	35
10–15 km	M	–	–	–	–	–	–
	IQM						
	IQR						

Table B8
Comparisons between CCI-GOMOS and lidar at Dumont D'Urville (shown are the median, IQM and IQR).

DUMONT D'URVILLE — Level 3							
E/B ratio		50 sr		30 sr		70 sr	
Altitude/version		2.19	3.00	2.19	3.00	2.19	3.00
22–27 km	M	−50	−56	−16	−26	−64	−68
	IQM	−32	−128	13	−146	−51	−120
	IQR	231	236	385	394	165	169
16–21 km	M	−23	−16	28	40	−45	−40
	IQM	21	27	102	111	−14	−10
	IQR	92	117	153	195	66	84
10–15 km	M	9	16	82	93	−22	−17
	IQM	21	151	102	319	−14	80
	IQR	148	193	247	322	106	138

For Garmisch-Partenkirchen (Table B6), an E/B value of 70 sr gives the best agreement between lidar and CCI-GOMOS time series, consistently with the Level 2 statistical analysis. The similarity between the results for version 2.19 and 3.00 is quite good.

In the case of Mauna Loa (Table B7), the level of agreement for the three choices of E/B is rather consistent with the case of Level 2. Overall, versions 2.19 and 3.00 give very similar results.

Finally, for Dumont d'Urville (Table B8), as for Level 2, there is no clear better choice between E/B values. In most cases, the results of the statistical analysis are similar for both CCI-GOMOS versions (2.19 and 3.00), especially when the median is used as statistical indicator.

B.3. E/B values for GOMOS/CALIOP

In order to get a better insight into the supposed variability of the E/B needed to convert the different lidar backscatter time series into extinction time series, we deduced the E/B values from the CCI-GOMOS and CALIOP datasets, both of them providing data on a global scale. This calculation was performed for three four-month time periods on the year 2008.

Table B9 shows E/B values for each considered time period (January–April, May–August and September–December 2008), three latitude bands between 50°S and 50°N and three altitude regions between 15 km and 30 km altitude. The median E/B values are calculated as the median of the ratio GOMOS/CALIOP. Values provided by Vernier et al. (2011b) for E/B, which are given for the same latitude/altitude range, are reproduced for comparison. Although the agreement is quite good at high altitude between Vernier et al. (2011b) and the present work, Vernier's estimates of E/B are overestimated with respect to the present work in all cases, the disagreement increasing with decreasing altitudes.

Table B9
Estimates of the extinction-to-backscatter ratio from the CCI-GOMOS dataset and the CALIOP dataset. The three values are calculated from Jan–Apr 2008, May–Aug 2008 and Sep–Dec 2008, respectively. In parentheses: estimate of the same quantity for the same latitude/altitude range by Vernier et al. (2011b).

E/B (sr)	50°S–20°S 01–04, 05–08, 09–12	20°S–20°N 01–04, 05–08, 09–12	20°N–50°N 01–04, 05–08, 09–12
15–20 km	34, 36, 43 (51)	41, 38, 42 (50)	28, 25, 24 (48)
20–25 km	45, 44, 45 (61)	50,50, 50 (64)	47, 42, 45 (58)
25–30 km	42,48, 48 (48)	46, 44, 53 (67)	41, 33, 48 (41)

Appendix C. Examples on the use of satellite and other data for the volcanic sulfur emission inventory

The aim of this appendix is to present some illustration on how the use of the CCI-GOMOS data record could improve the detection of moderate volcanic eruptions, and the quantification of their sulfur emissions. Two examples are provided: the case of the eruption of Reventador on 3rd November 2002, and the case of Piton de la Fournaise on 6th April 2007.

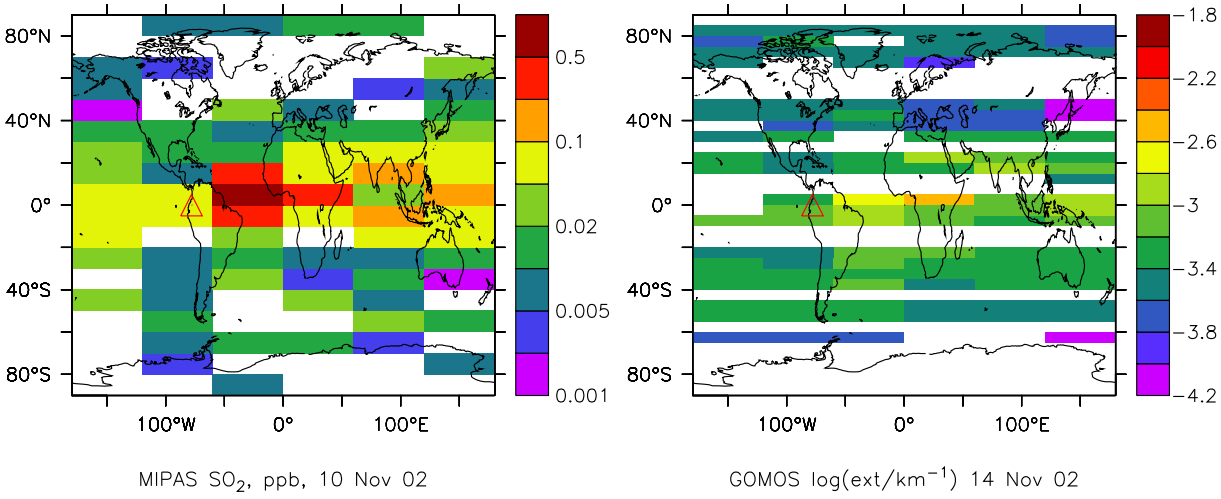

Fig. C-1. The eruption of Reventador on 3rd November 2002: MIPAS SO_2 concentration (left panel) and CCI-GOMOS aerosol extinction (right panel) at 17 km altitude.

The SO_2 emissions of the eruption of Reventador in Ecuador on 3rd November 2002 (VEI 4) are visible on MIPAS satellite images some days after the eruption. Entries in the Bulletin Reports of the Smithsonian Institution documented "a column rose up to 16–17 km above the intracaldera cone". So the plume was injected directly into the stratosphere and was transported very fast by westerly winds from Ecuador to Africa and Indonesia. This plume is also visible on satellite images from GOMOS, TOMS, and AIRS. For the entry in Table 7 we use the MIPAS-data of 5-day intervals centered on 10th and 15th November.

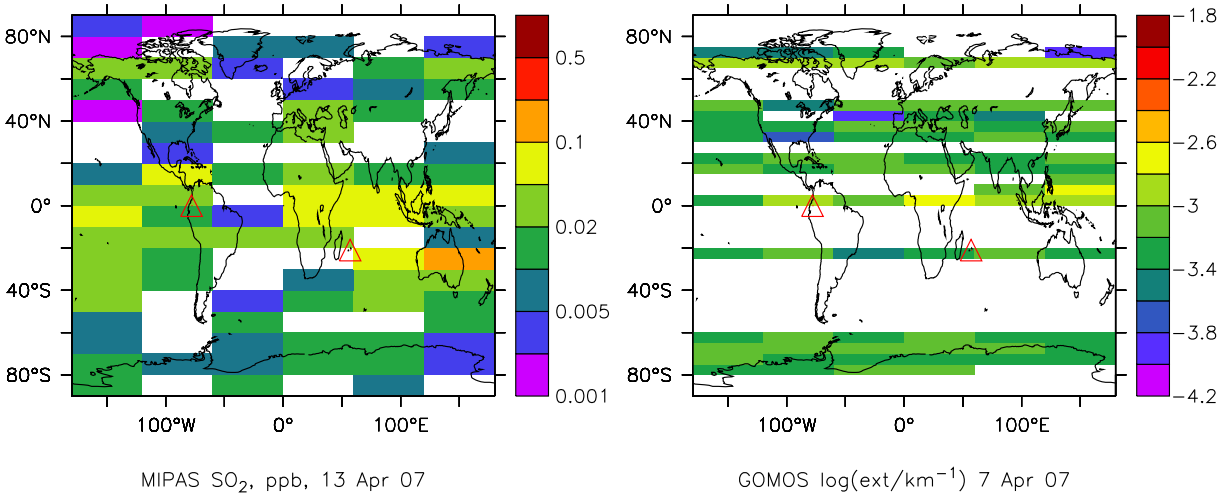

Fig. C-2. Same as in Fig. C-1 for the eruption of Piton de la Fournaise on 6th April 2007.

The eruption of Piton de la Fournaise starting on 6th April 2007 was not visible in the MIPAS data on the date of the eruption, because of a data gap in this 5-day time interval. The next accessible data is the time interval on 13th April with a signal above Australia and the Indian Ocean. By comparison with GOMOS data on 7th April, it is possible to identify the eruption of Piton de la Fournaise on the island Reunion east of Madagascar, several thousand kilometers away from the MIPAS signal above Australia. This is confirmed by other satellite data of OMI and GOME2. Entries in the Bulletin Reports of the Smithsonian Institution documented a caldera collapse on 6th April and ongoing volcanic activity for one month contributing to the observed SO_2 plumes. For calculation, we used an integral on three time-intervals centered on 3, 13 and 18th April derived from the 3D MIPAS data sets. In the data of both instruments also plumes near Colombia are visible which can be attributed to Reventador. Therefore, the entry for this event in Table 7 includes 2 partial integrals, contributions from both eruptions.

References

Antuña, J.C., Robock, A., Stenchikov, G., Zhou, J., David, C., Barnes, J., Thomason, L., 2003. Spatial and temporal variability of the stratospheric aerosol cloud produced by the 1991 Mount Pinatubo eruption. J. Geophys. Res. 108:4624, D20. http://dx.doi.org/10.1029/2003JD003722.

Astitha, M., Lelieveld, J., Abdel Kader, M., Pozzer, A., de Meij, A., 2012. Parameterization of dust emissions in the global atmospheric chemistry-climate model EMAC: impact of nudging and soil properties. Atmos. Chem. Phys. 12:11057–11083. http://dx.doi.org/10.5194/acp-12-11057-2012.

Barnes, J.E., Hofmann, D.J., 1997. Lidar measurements of stratospheric aerosol over Mauna Loa Observatory. Geophys. Res. Lett. 24:1923–1926. http://dx.doi.org/10.1029/97GL01943.

Barnes, J.E., Hofmann, D.J., 2001. Variability in the stratospheric background aerosol over Mauna Loa Observatory. Geophys. Res. Lett. 28:2895–2898. http://dx.doi.org/10.1029/2001GL013127.

Bertaux, J.-L., Kyrölä, E., Fussen, D., Hauchecorne, A., Dalaudier, F., Sofieva, V., Tamminen, J., Vanhellemont, F., Fanton d'Andon, O., Barrot, G., et al., 2010. Global ozone monitoring by occultation of stars: an overview of GOMOS measurements on ENVISAT. Atmos. Chem. Phys. 10, 12091–12148.

Bourassa, A.E., Degenstein, D.A., Gattinger, R.L., Llewellyn, E.J., 2007. Stratospheric aerosol retrieval with optical spectrograph and infrared imaging system limb scatter measurements. J. Geophys. Res. 112, D10217. http://dx.doi.org/10.1029/2006JD008079.

Brühl, C., Lelieveld, J., Crutzen, P.J., Tost, H., 2012. The role of carbonyle sulphide as a source of stratospheric sulphate aerosol and its impact on climate. Atmos. Chem. Phys. 12:1239–1253. http://dx.doi.org/10.5194/acp-12-1239-2012.

Brühl, C., Lelieveld, J., Tost, H., Höpfner, M., Glatthor, N., 2015. Stratospheric sulphur and its implications for radiative forcing simulated by the chemistry climate model EMAC. J. Geophys. Res. Atmos. 120:2103–2118. http://dx.doi.org/10.1002/2014JD022430.

Chazette, P., David, C., Lefrère, J., Godin, S., Pelon, J., Mégie, G., 1995. Comparative lidar study of the optical, geometrical, and dynamical properties of stratospheric post-volcanic aerosols, following the eruptions of El Chichon and Mount Pinatubo. J. Geophys. Res. 100 (D11):23195–23207. http://dx.doi.org/10.1029/95JD02268.

Chen, W.N., Chiang, C.W., Nee, J.B., 2002. Lidar ratio and depolarization ratio for cirrus clouds. Appl. Opt. 31, 6470–6476.

Collis, R.T.H., Russell, P.B., 1976. In: Hinkley, E.D. (Ed.), Lidar Measurement of Particles and Gases by Elastic Backscattering and Differential Absorption. Laser Monitoring of the Atmosphere. Springer Verlag.

David, C., Haefele, A., Keckhut, P., Marchand, M., Jumelet, J., Leblanc, T., Cenac, C., Laqui, C., Porteneuve, J., Haeffelin, M., Courcoux, Y., Snels, M., Viterbini, M., Quatrevalet, M., 2012. Evaluation of stratospheric ozone, temperature, and aerosol profiles from the LOANA lidar in Antarctica. Pol. Sci. 6 (3–4):209–225. http://dx.doi.org/10.1016/j.polar.2012.07.001.

GCOS, 2009. Guideline for the Generation of Satellite-based Datasets and Products Meeting GCOS Requirements. GCOS-128, WMO/TD No. 1488. WMO, Geneva, Switzerland.

GCOS, 2011. Systematic Observation Requirements for Satellite-Based Data Products for Climate; 2011 Update, Supplemental Details to the Satellite-Based Component of the "Implementation Plan for the Global Observing System for Climate in Support of the UNFCCC (2010 Update)". GCOS-154. Geneva, Switzerland, WMO.

Grainger, R.G., Lambert, A., Rodgers, C.D., Taylor, F.W., Deshler, T., 1995. Stratospheric aerosol effective radius, surface area and volume estimated from infrared measurements. J. Geophys. Res. 100, 16,507–16,518.

Hofmann, D., Barnes, J., O'Neill, M., Trudeau, M., Neely, R., 2009. Increase in background stratospheric aerosol observed with lidar at Mauna Loa Observatory and Boulder, Colorado. Geophys. Res. Lett. 36, L15808. http://dx.doi.org/10.1029/2009GL039008.

Hollmann, R., Merchant, C.J., Saunders, R., Downy, C., Buchwitz, M., Cazenave, A., Chuvieco, E., Defourny, P., de Leeuw, G., Forsberg, R., Holzer-Popp, T., Paul, F., Sandven, S., Sathyendranath, S., van Roozendael, M., Wagner, W., 2013. The ESA climate change initiative: satellite data records for essential climate variables. Bull. Am. Meteorol. Soc. 1541–1552 Oct. 2013. e-View. http://dx.doi.org/10.1175/BAMS-D-11-00254.1.

Höpfner, M., Glatthor, N., Grabowski, U., Kellmann, S., Kiefer, M., Linden, A., Orphal, J., Stiller, G., von Clarmann, T., Funke, B., Boone, C.D., 2013. Sulfur dioxide (SO_2) as observed by MIPAS/Envisat: temporal development and spatial distribution at 15–45 km altitude. Atmos. Chem. Phys. 13, 10405–10423.

Höpfner, M., Boone, C.D., Funke, B., Glatthor, N., Grabowski, U., Günther, A., Kellmann, S., Kiefer, M., Linden, A., Lossow, S., Pumphrey, H.C., Read, W.G., Roiger, A., Stiller, G., Schlager, H., von Clarmann, T., Wissmüller, K., 2015. Sulfur dioxide (SO_2) from MIPAS in the upper troposphere and lower stratosphere 2002–2012. Atmos. Chem. Phys. 15, 7017–7037.

Jäger, H., 2005. Long-term record of lidar observations of the stratospheric aerosol layer at Garmisch-Partenkirchen. J. Geophys. Res. 110, D08106. http://dx.doi.org/10.1029/2004JD005506.

Jäger, H., Deshler, T., 2002. Lidar backscatter to extinction, mass and area conversions for stratospheric aerosols based on midlatitude balloonborne size distribution measurements. Geophys. Res. Lett. 29 (19):1929. http://dx.doi.org/10.1029/2002GL015609.

Jäger, H., Deshler, T., Hofmann, D.J., 1995. Midlatitude lidar backscatter conversions based on balloon-borne aerosol measurements. Geophys. Res. Lett. 22:1729–1732. http://dx.doi.org/10.1029/95GL01521.

Jöckel, P., Tost, H., Pozzer, A., Brühl, C., Buchholz, J., Ganzeveld, L., Hoor, P., Kerkweg, A., Lawrence, M.G., Sander, R., Steil, B., Stiller, G., Tanarhte, M., Taraborrelli, D., van Aardenne, J., Lelieveld, J., 2006. The atmospheric chemistry general circulation model ECHAM5/MESSy1: consistent simulation of ozone from the surface to the mesosphere. Atmos. Chem. Phys. 6, 5067–5104.

Jöckel, P., Kerkweg, A., Pozzer, A., Sander, R., Tost, H., Riede, H., Baumgaertner, A., Gromov, S., Kern, B., 2010. Development cycle 2 of the Modular Earth Submodel System (MESSy2). Geosci. Model Dev. 3:717–752. http://dx.doi.org/10.5194/gmd-3-717-2010.

Kremser, S., Thomason, L.W., von Hobe, M., Hermann, M., Deshler, T., et al., 2016. Stratospheric aerosol—observations, processes, and impact on climate. Rev. Geophys. 54: 278–335. http://dx.doi.org/10.1002/2015RG000511.

Kyrölä, E., Tamminen, J., Sofieva, V., Bertaux, J.L., Hauchecorne, A., Dalaudier, F., Fussen, D., Vanhellemont, F., Fanton d'Andon, O., Barrot, G., et al., 2008. Retrieval of atmospheric parameters from GOMOS data. Atmos. Chem. Phys. 10, 11881–11903.

Kyrölä, E., Tamminen, J., Sofieva, V., Bertaux, J.L., Hauchecorne, A., Dalaudier, F., Fussen, D., Vanhellemont, F., Fanton d'Andon, O., Barrot, G., et al., 2010. GOMOS O_3, NO_2, and NO_3 observations in 2002–2008. Atmos. Chem. Phys. 10, 7723–7738.

Noel, V., Hertzog, A., Chepfer, H., 2009. CALIPSO observations of wave-induced PSCs with near-unity optical depth over Antarctica in 2006–2007. J. Geophys. Res. 114, D05202. http://dx.doi.org/10.1029/2008JD010604.

Orphal, J., Fellows, C.E., Flaud, P.-M., 2003. The visible absorption spectrum of NO3 measured by high-resolution Fourier transform spectroscopy. J. Geophys. Res. 108 (D3): 4077. http://dx.doi.org/10.1029/2002JD002489.

Popp, T., de Leeuw, G., Bingen, C., Brühl, C., Capelle, V., Chedin, A., Clarisse, L., Dubovik, O., Grainger, R., Griesfeller, J., et al., 2016. Development, production and evaluation of aerosol climate data records from European satellite observations (Aerosol_cci). Remote Sens. 8:421. http://dx.doi.org/10.3390/rs8050421.

Reichardt, J., Dörnbrack, A., Reichardt, S., Yang, P., McGee, T.J., 2004. Mountain wave PSC dynamics and microphysics from ground-based lidar measurements and meteorological modeling. Atmos. Chem. Phys. 4:1149–1165. http://dx.doi.org/10.5194/acp-4-1149-2004.

Robert, C.E., Bingen, C., Vanhellemont, F., Mateshvili, N., Dekemper, E., Tétard, C., Fussen, D., Zehner, C., Thomason, L.W., McElroy, C.T., et al., 2016. AerGOM, an improved algorithm for stratospheric aerosol extinction retrieval from GOMOS observations part 2: intercomparisons. Atmos. Meas. Tech. 9:4701–4718. http://dx.doi.org/10.5194/amt-9-4701-2016.

Rosen, J., Hofmann, D.J., 1986. Optical modelling of stratospheric aerosols: present status. Appl. Opt. 25, 410–419.

Sander, S.P., 1986. Temperature dependence of the NO_3 absorption spectrum. J. Phys. Chem. 90, 4135–4142.

von Savigny, C., Ernst, F., Rozanov, A., Hommel, R., Eichmann, K.-U., Rozanov, V., Burrows, J.P., Thomason, L.W., 2015. Improved stratospheric aerosol extinction profiles from SCIAMACHY: validation and sample results. Atmos. Meas. Tech. 8, 5223–5235.

Serdyuchenko, A., Gorshelev, V., Weber, M., Chehade, W., Burrows, J.P., 2014. High spectral resolution ozone absorption cross-sections — part 2: temperature dependence. Atmos. Meas. Tech. 7:625–636. http://dx.doi.org/10.5194/amt-7-625-2014.

Sofieva, V., Kan, V., Dalaudier, F., 2009. Influence of scintillation on quality of ozone monitoring by GOMOS. Atmos. Chem. Phys. 9, 9197–9207.

Solomon, S., Daniel, J.S., Neely III, R.R., Vernier, J.-P., Dutton, E.G., Thomason, L.W., 2011. The persistently variable "background" stratospheric aerosol layer and global climate change. Science 333, 866–870.

SPARC, 2006. In: Thomason, L., Peter, Th. (Eds.), Report No. 4: Assessment of Stratospheric Aerosol Properties (ASAP). World Climate Research Programme Report WCRP-124/WMO/TD-No. 1295, WMO/ICSU/IOC. http://www.sparc-climate.org/publications/sparc-reports/.

SPARC, 2017. In: Hegglin, M.I., Tegtmeier, S. (Eds.), Report No.8: The SPARC Data Initiative: Assessment of Stratospheric Trace Gas and Aerosol Climatologies From Satellite Limb Sounders WCRP-05/2017. http://dx.doi.org/10.3929/ethz-a-010863911 www.sparc-climate.org/publications/sparc-reports/.

Steinbrecht, W., Jäger, H., Adriani, A., di Donfrancesco, G., Barnes, J., Beyerle, G., Neuber, R., David, C., Godin, S., Donovan, D., Carswell, A.I., Gross, M., McGee, T., Masci, F., D'Altorio, A., Rizi, V., Visconti, G., McDermid, I.S., Megie, G., Mielke, A., Stein, B., Wedekind, C., Nagai, T., Uchino, O., Nakane, H., Osborn, M., Winker, D., 1997. NDSC Intercomparison of Stratospheric Aerosol Processing Algorithms, Advances in Atmospheric Remote Sensing With Lidar. Springer, New York-Berlin-Heidelberg: pp. 501–504 http://dx.doi.org/10.1007/978-3-642-60612-0_121.

Trickl, T., Giehl, H., Jäger, H., Vogelmann, H., 2013. 35 yr of stratospheric aerosol measurements at Garmisch-Partenkirchen: from Fuego to Eyjafjallajökull, and beyond. Atmos. Chem. Phys. 13:5205–5225. http://dx.doi.org/10.5194/acp-13-5205-2013.

Vandaele, A.C., Hermans, C., Simon, P.C., Carleer, M., Colin, R., Fally, S., Mérienne, M.-F., Jenouvrier, A., Coquart, B., 1998. Measurements of the NO_2 absorption cross-section from 42,000 cm^{-1} to 10,000 cm^{-1} (238–1000 nm) at 220 K and 294 K. JQSRT 59, 171–184.

Vandaele, A.C., Hermans, C., Simon, P.C., Carleer, M., Colin, R., Fally, S., Mérienne, M.-F., Jenouvrier, A., Coquart, B., 2002. High-resolution Fourier transform measurement of the NO_2 visible and near-infrared absorption cross-section: temperature and pressure effects. J. Geophys. Res. 107 (D18):4348. http://dx.doi.org/10.1029/2001JD000971.

Vandaele, A.C., Hermans, C., Fally, S., Carleer, M., Mérienne, M.-F., Jenouvrier, A., Coquart, B., Colin, R., 2003. Absorption cross-section of NO_2: simulation of temperature and pressure effects. JQSRT 76, 373–391.

Vanhellemont, F., Tétard, C., Bourassa, A., Fromm, M., Dodion, J., Fussen, D., Brogniez, C., Degenstein, D., Gilbert, K.L., Turnbull, D.N., Bernath, P., Boone, C., Walker, K.A., 2008. Aerosol extinction profiles at 525 nm and 1020 nm derived from ACE imager data: comparisons with GOMOS, SAGE II, SAGE III, POAM III, and OSIRIS. Atmos. Chem. Phys. 8, 2027–2037.

Vanhellemont, F., Mateshvili, N., Blanot, L., Robert, C.E., Bingen, C., Tétard, C., Fussen, D., Dekemper, E., Sofieva, V., Kyrölä, E., et al., 2016. AerGOM, an improved algorithm for stratospheric aerosol extinction retrieval from GOMOS observations part 1: algorithm development. Atmos. Meas. Tech. 9:4687–4700. http://dx.doi.org/10.5194/amt-9-4687-2016.

Vernier, J.-P., Pommereau, J.-P., Garnier, A., Pelon, J., Larsen, N., Nielsen, J., Christensen, T., Cairo, F., Thomason, L.W., Leblanc, T., McDermid, I.S., 2009. Tropical stratospheric aerosol layer from CALIPSO lidar observations. J. Geophys. Res. 114, D00H10. http://dx.doi.org/10.1029/2009JD011946.

Vernier, J.P., Thomason, L.W., Kar, J., 2011a. CALIPSO detection of an Asian tropopause aerosol layer. Geophys. Res. Lett. 38, L07804. http://dx.doi.org/10.1029/2010GL046614.

Vernier, J.-P., Thomason, L.W., Pommereau, J.-P., Bourassa, A., Pelon, J., et al., 2011b. Major influence of tropical volcanic eruptions on the stratospheric aerosol layer during the last decade. Geophys. Res. Lett. 38, L12807. http://dx.doi.org/10.1029/2011GL047563.

Vernier, J.-P., Fairlie, T.D., Natarajan, M., Wienhold, F.G., Bian, J., 2015. Increase in upper tropospheric and lower stratospheric aerosol levels and its potential connection with Asian pollution. J. Geophys. Res. Atmos.:120 http://dx.doi.org/10.1002/2014JD022372.

Wang, J., Park, S., Zeng, J., Ge, C., Yang, K., Carn, S., Krotkov, N., Omar, A.H., 2013. Modeling of 2008 Kasatochi volcanic sulfate direct radiative forcing: assimilation of OMI SO_2 plume height data and comparison with MODIS and CALIOP observations. Atmos. Chem. Phys. (13):1895–1912 http://dx.doi.org/10.5194/acp-13-1895-2013.

Winker, D.M., Vaughan, M., Omar, A., Hu, Y., Powell, K., Liu, Z., Hunt, W., Young, S.A., 2009. Overview of the CALIPSO mission and CALIOP data processing algorithms. J. Atmos. Ocean. Technol. 26:2310–2323. http://dx.doi.org/10.1175/2009JTECHA1281.1.

Yokelson, R.J., Burkholder, J.B., Fox, R.W., Talukdar, R.K., Ravishankara, A.R., 1994. Temperature dependence of the NO_3 absorption spectrum. J. Phys. Chem. 98, 13.144–13.150.

Yu, P., Murphy, D.M., Portmann, R.W., Toon, O.B., Froyd, K.D., Rollins, A.W., Gao, R.-S., Rosenlof, K.H., 2016. Radiative forcing from anthropogenic sulfur and organic emissions reaching the stratosphere. Geophys. Res. Lett. 43:9361–9367. http://dx.doi.org/10.1002/2016GL070153.